JCB Journal of Cell Biology

REPORT

Hematopoietic progenitors polarize in contact with bone marrow stromal cells in response to SDF1

Thomas Bessy[1,2*], Adrian Candelas[1,2*], Benoit Souquet[1,2,3], Khansa Saadallah[1,2], Alexandre Schaeffer[1,2], Benoit Vianay[1,2], Damien Cuvelier[4,5,6], Samy Gobaa[7], Cecilia Nakid-Cordero[8], Julien Lion[8], Jean-Christophe Bories[8], Nuala Mooney[8], Thierry Jaffredo[9], Jerome Larghero[10], Laurent Blanchoin[1,2], Lionel Faivre[10], Stephane Brunet[1,2], and Manuel Théry[1,2]

The fate of hematopoietic stem and progenitor cells (HSPCs) is regulated by their interaction with stromal cells in the bone marrow. However, the cellular mechanisms regulating HSPC interaction with these cells and their potential impact on HSPC polarity are still poorly understood. Here we evaluated the impact of cell–cell contacts with osteoblasts or endothelial cells on the polarity of HSPC. We found that an HSPC can form a discrete contact site that leads to the extensive polarization of its cytoskeleton architecture. Notably, the centrosome was located in proximity to the contact site. The capacity of HSPCs to polarize in contact with stromal cells of the bone marrow appeared to be specific, as it was not observed in primary lymphoid or myeloid cells or in HSPCs in contact with skin fibroblasts. The receptors ICAM, VCAM, and SDF1 were identified in the polarizing contact. Only SDF1 was independently capable of inducing the polarization of the centrosome–microtubule network.

Introduction

Hematopoietic stem cells (HSCs) are at the origin of all blood lineages (Orkin and Zon, 2008). In the liver of the fetus, or in the bone marrow of an adult, hematopoietic stem and progenitor cells (HSPCs) sense and respond to numerous biochemical stimuli (Pinho and Frenette, 2019). Within the bone marrow, the vascular network and the bone matrix constitute local niches that impart distinct and specific signals regulating the quiescence, proliferation, and differentiation of HSPCs (Morrison and Scadden, 2014; Christodoulou et al., 2020; Guezguez et al., 2013). Perturbed interactions between HSPCs and their niches have been associated with blood malignancies and aging (Verovskaya et al., 2019), underscoring the importance of better understanding how HSPCs sense and respond to stromal and endothelial cells in the bone marrow (Ceafalan et al., 2018).

Several lines of experimental evidence, in living organisms and in cultured cells, have revealed that, in addition to diffusible signals, direct cell-to-cell contact is involved in the regulation of HSPC fate (Wagner et al., 2007; Bruns et al., 2014; Alakel et al., 2009; Ceafalan et al., 2018; Walenda et al., 2010). In cocultures of human CD34$^+$, HSPCs isolated from newborn cord blood and mesenchymal stromal cells from bone marrow aspirates (Wagner et al., 2007), HSPCs can adopt elongated and asymmetric morphologies, with several types of protrusions of various lengths and widths (Francis et al., 1998) that can have specific impact on proliferation and differentiation (Freund et al., 2006; Frimberger et al., 2001; Holloway et al., 1999). Similar polarized HSPC morphologies have also been observed in vivo (Coutu et al., 2017), but the stromal cells and signaling pathways that give rise to these morphologies remain to be deciphered.

In addition to a polarized morphology, HSPCs can polarize biochemically, as characterized by the accumulation of membrane-associated proteins in the protrusions forming either at the side in contact with the stromal cells (Freund et al., 2006; Wagner et al., 2008) or at the opposite side (Görgens et al., 2012; Fonseca et al., 2010). This polarization of membrane markers has been

[1]Cytomorpho Lab, Human Immunology, Pathophysiology, Immunotherapy, Unit 976, Institut National de la Santé et de la Recherche Médicale, CEA, Assistance Publique – Hôpitaux de Paris, Université de Paris, Institut de Recherche Saint Louis, Paris, France; [2]Cytomorpho Lab, Laboratoire Physiologie Cellulaire et Végétale, UMR 5168, CEA, Institut national de recherche en agriculture, alimentation et environment, Centre national de la recherche scientifique, Université Grenoble-Alpes, Interdisciplinary Research Institute of Grenoble, Grenoble, France; [3]Alveole, Paris, France; [4]Sorbonne Université, Paris, France; [5]Institut Pierre Gilles de Gennes, Paris Sciences et Lettres Research University, Paris, France; [6]Institut Curie, Paris Sciences et Lettres Research University, Centre national de la recherche scientifique, UMR 144, Paris, France; [7]Group of Biomaterials and Microfluidics Core Facility, Institut Pasteur, Paris, France; [8]Human Immunology, Pathophysiology, Immunotherapy, Unit 976, Institut National de la Santé et de la Recherche Médicale, Université de Paris, Institut de Recherche Saint Louis, Paris, France; [9]Laboratoire de Biologie du Développement, Centre national de la recherche scientifique, UMR 7622, Institut National de la Santé et de la Recherche Médicale U1156, Sorbonne Université, Institut de Biologie Paris-Seine, Paris, France.; [10]Unité de Thérapie Cellulaire, Human Immunology, Pathophysiology, Immunotherapy, Unit 976, Assistance Publique – Hôpitaux de Paris, Hôpital Saint-Louis, Center of Clinical Investigations in Biotherapies of Cancer CBT501, Institut National de la Santé et de la Recherche Médicale, Université de Paris, Paris, France.

*T. Bessy and A. Candelas contributed equally to this paper; Correspondence to Stephane Brunet: stephane.brunet@inserm.fr; Manuel Théry: manuel.thery@cea.fr.

mostly described in the case of migrating HSPCs (Fonseca and Corbeil, 2011). Indeed, the segregated molecules and the associated signaling pathways are in many ways similar to the uropod of a migrating lymphocyte or neutrophil and include the rearward localization of the centrosome (Sánchez-Madrid and Serrador, 2009; Fonseca et al., 2010; Heasman et al., 2010). However, the uropod is also involved in cell–cell interactions in T lymphocytes (Sánchez-Madrid and Serrador, 2009) and HSPCs (Wagner et al., 2008), suggesting that not only migration but also anchorage could involve HSPCs polarization. In support of this hypothesis, localized adhesion-associated signaling and exchange of endosomes between HSPCs and osteoblasts have suggested the existence of synapse-like interactions (Gillette et al., 2009), as is the case for many stem cells interacting with the cells forming their niche (Wilson and Trumpp, 2006; Ceafalan et al., 2018). However, the cellular mechanism inducing the polarization of HSPCs in response to their adhesion to stromal cells has not yet been investigated in detail. Furthermore, the similarities and differences between the polarities of migrating and anchored HSPCs are still unclear. Such investigations appear all the more necessary in that it has recently been revealed that quiescent long-term HSCs are actually nonmotile in vivo (Christodoulou et al., 2020). Although a lot has been learned from coculture experiments, it has remained technically challenging to study the specific role of cell adhesion independently of cell migration.

Results

In the bone marrow, hematopoietic progenitors encounter a large diversity of microenvironments, where diverse sets of stromal cells secrete specific cytokines and present specific intercellular adhesion receptors at their surface (Pinho and Frenette, 2019). In the endosteal niche, close to the bone matrix, osteoblasts interact directly with HSPCs and thereby promote HSPC quiescence and long-term self-renewal capacities (Bowers et al., 2015; Jung et al., 2005; Guezguez et al., 2013; Calvi et al., 2003). By contrast, in the perivascular niches, close to blood veins and arteries, endothelial cells and pericytes stimulate HSPC proliferation and differentiation (Kopp et al., 2005; Kiel et al., 2005; Ding et al., 2012; Greenbaum et al., 2013; Asada et al., 2017). To investigate the molecular and cellular mechanisms underlying these activities, we designed a microfluidic bone-marrow-on-a-chip model of the HPSC niche (Ingavle et al., 2019; Chou et al., 2020; Sieber et al., 2018). The model was inspired by the pioneering work of Noo-Li Jeon, who described the setup for the microchannel geometry and the culture conditions necessary for inducing endothelial cell self-organization into hollow and perfusable 3D networks (Kim et al., 2013). Side channels included osteoblasts in 3D matrices made of collagen and fibrin to model a minimal version of the endosteal niche (Nelson et al., 2021). Maskless photolithography was used to test several chip prototypes and optimize channel design, which included the presence of pillars preventing the collapse of the 3D matrix in response to high contractile forces produced by osteoblasts (see Materials and methods; Souquet et al., 2021). Human HSPCs ($CD34^+$ from newborn cord blood) were loaded in a central channel with the same 3D matrix as in the side channels (Fig. 1 A), so that they could migrate in 3D and enter those side channels (Fig. 1 B and Video 1).

Importantly, the bone-marrow-on-a-chip model was compatible with chemical fixation, immunolabeling, and high-magnification imaging. HSPCs were identified by CD34 immunostaining (Fig. 1 C). HSPCs displayed both round and polarized shapes in contact with either osteoblasts or endothelial cells (Fig. 1 C), as found in vivo (Coutu et al., 2017). Contacts between HSPCs and both types of stromal cells were imaged in 3D to capture all orientations. The microtubule-organization center of HSPCs was observed toward the site of contact, toward the opposite side, or in an intermediate position (Fig. 1 D). However, microtubule-organization centers were more frequently observed toward the contact site, whether HSPCs were in contact with osteoblasts or endothelial cells (Fig. 1 D). Although HSPCs displayed some clear and characteristic polarized organization, it was unclear whether this polarization was due to the cell–cell interaction per se and not to the HPSCs' high propensity to migrate in the 3D model (Souquet et al., 2021).

To study the specific role of the contact between an HSPC and a bone marrow niche cell, we developed a culture model that promoted long-term cell–cell interactions but prevented cell migration. Various sorts of microwells have been engineered to confine distinct cell types in a common volume (Dusseiller et al., 2005; Khademhosseini et al., 2006; Moeller et al., 2008; Lutolf et al., 2009; Guldevall et al., 2010; Minc et al., 2011; Gobaa et al., 2011; Müller et al., 2015). In such microwells, HSPC stemness could be maintained over several weeks in 3D cocultures with mesenchymal stromal cells (Wuchter et al., 2016). In our culture model, we used a differential patterning approach to restrict cell-substrate adhesion to the bottom of the microwell only, to prevent cells from escaping the well (Dusseiller et al., 2005; Ochsner et al., 2007; Gobaa et al., 2011) and to enable high-quality imaging. This approach required a new fabrication protocol combining glass silanization and polyacrylamide (PAA) capillary-based molding using nonadhesive microwells with glass bottoms (see Materials and methods and Fig. S1 A).

HSPCs were cultured at ∼1 cell per 50-µm-wide microwell already seeded with a single osteoblast. As expected, HSPCs interacted with the dorsal surface of the osteoblast (Fig. 2 A). Long-term imaging showed that HSPCs proliferated at a normal rate, suggesting that the microwell manufacturing was not toxic (Fig. 2 B). Furthermore, HSPCs were occasionally observed to migrate, locate below the osteoblasts, and proliferate, forming what has been termed a cobblestone structure that is typical of HSCs in long-term cultures (Jing et al., 2010; Fig. 2 C), further suggesting that the HSPCs were healthy. Certain HSPCs were observed by video recording to attach to migrating osteoblasts, showing that this coculture model permitted the formation of strong heterotypic cell–cell contacts (Fig. 2 D), as previously found in other models (Wagner et al., 2007). Interestingly, HSPCs attached to osteoblasts via a small but strong anchorage site that resisted cell migration despite dynamic shape changes (Video 2). Attached HSPCs adopted elongated and asymmetric shapes (Fig. 2 E) similar to those observed in 3D conditions in the bone-marrow-on-a-chip model (Fig. 1 E), as well as in bone

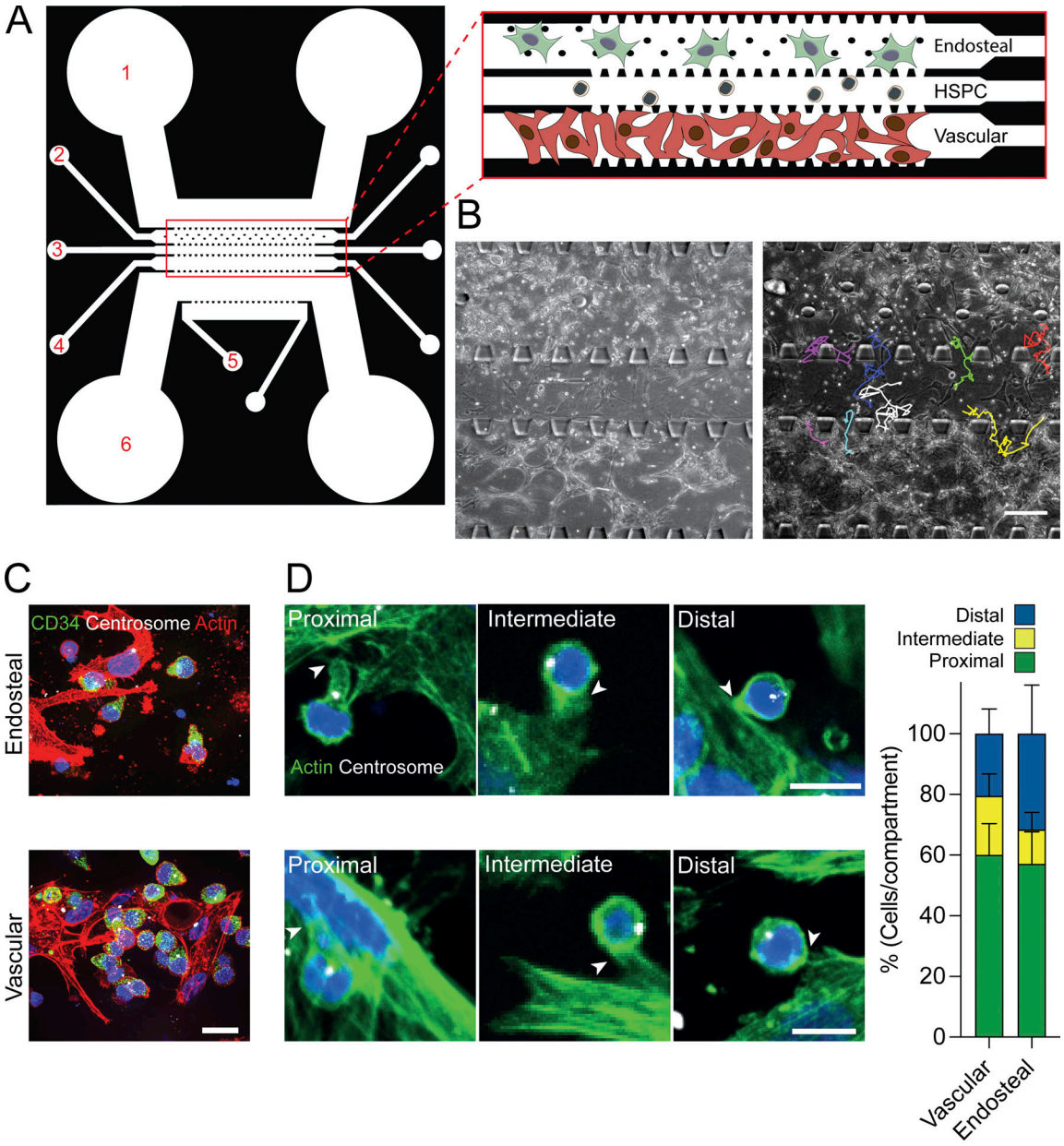

Figure 1. **Bone-marrow-on-a-chip allows the monitoring of HSPCs in contact with mesenchymal stem cells in 3D hydrogels. (A)** Plan of the microfluidic chip: it comprises the endosteal (2) and the vascular (4) compartments, the HSPC injection channel (3), the cytokine-secreting fibroblast compartment (5), and channels for medium circulation (1 and 6). The inset describes the organization of the central channels loaded with cells. **(B)** Left: Transmitted light image of the three central channels. Right: Colorized individual trajectories of HSPCs during a time-lapse sequence. Scale bar = 200 µm. **(C)** Maximum projection of 10-µm-wide Z stack confocal images of HSPCs in the endosteal (upper panel) and vascular (lower panel) compartments. HSPCs ($CD34^+$) appear in green, actin structures in red, DNA in blue, and centrosomes in white. Scale bar = 10 µm. **(D)** Selected Z stacks of HSPCs in the endosteal and vascular compartments are presented in the upper and lower panel, respectively. The HSPC centrosome can be defined relative to the point of contact of the HSPC with the osteoblast or endothelial cell (marked with a white arrow) as proximal (left), in an intermediate position (middle), or distal (right). Actin appears in green, centrosome in white, and DNA in blue. Scale bar = 10 µm. Right: Distribution of HSPCs with proximal, intermediate, or distal centrosome in the vascular (n = 73) and endosteal (n = 199) compartments from three independent experiments. Error bars represent SD.

marrow in vivo (Coutu et al., 2017). HSPCs appeared to be attached to stromal cells by a pseudopod of variable size that has been previously described and named a "magnupodium" (Francis et al., 1998; Freund et al., 2006), similar to the stalk-like projection documented in B lymphoblastoid cells (Dustin et al., 1992). The contact site of this magnupodium was restricted to a small area estimated to be ∼1–2 µm². However, in contrast to a lymphocyte forming an immune synapse on a target cell (Ritter et al., 2013), HSPCs were not observed to spread on osteoblasts.

The entire architecture of HSPCs in contact with osteoblasts appeared to be highly polarized (Fig. 3 A). In particular, the centrosome was typically observed at the tip of the magnupodium, in close proximity with the contact site (Fig. 3, A–C and F; reconstitution in Video 3). The Golgi adopted an elongated shape

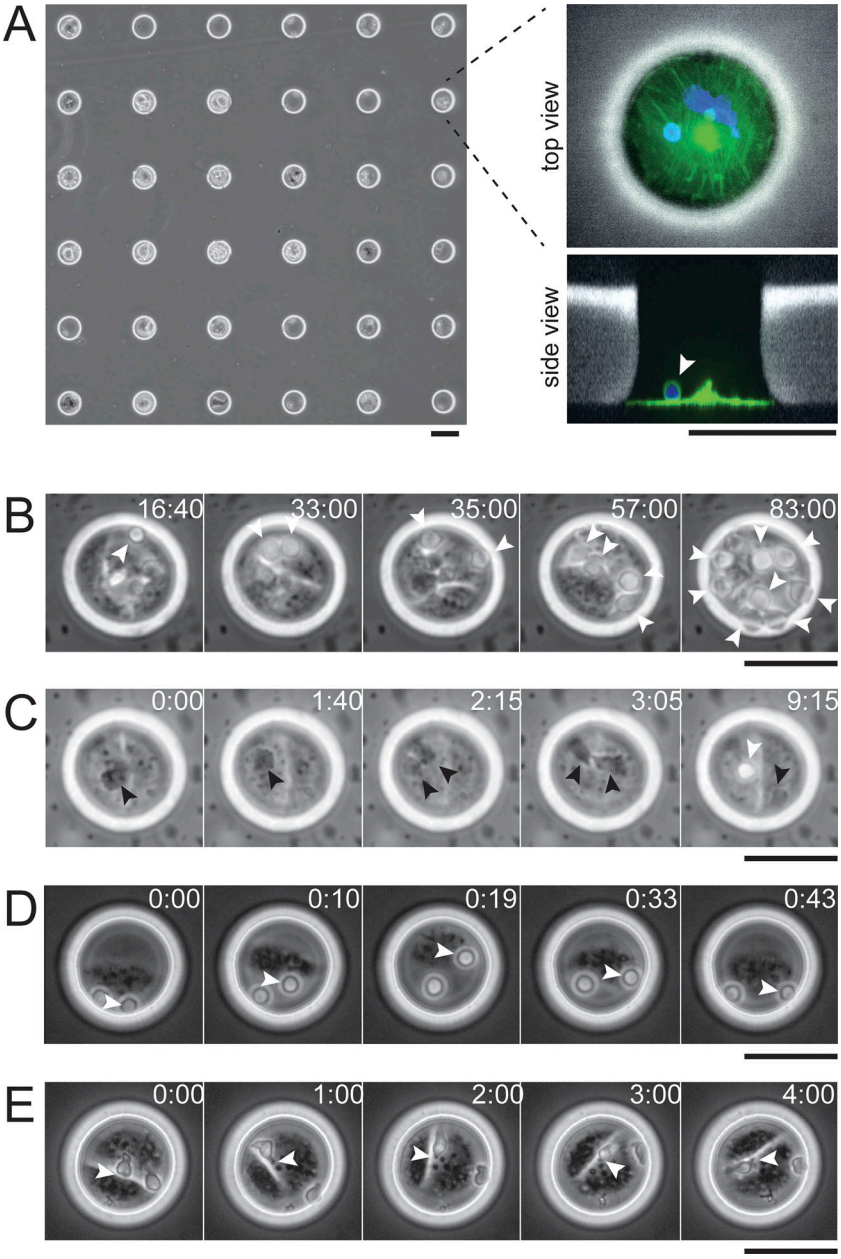

Figure 2. **Array of microwells to control HSPC–mesenchymal stem cell interaction. (A)** Transmitted light images of the PAA stencil showing the 50-µmwide circular holes seeded with osteoblasts and HSPCs (left). Images of top (upper right) and side (lower right) views of a single microwell containing fixed cells, stained for tubulin in green and DNA in blue. Fluorescent dextran was incorporated in the PAA mix to reveal the microwell (white). HSPCs were identified by small size and round shape (white arrowhead), whereas osteoblasts were larger and spread at the bottom of the microwell. **(B–E)** Time-lapse monitoring with transmitted light of live HSPCs (white arrowheads) in contact with osteoblasts (time indicated in hours:minutes). **(B)** Representative image of HSPC in proliferation. **(C)** Representative image of HSPC engaged in migration and confinement below osteoblasts (highlighted with black arrowheads). **(D)** Representative HSPC engaged in adhesion onto a moving osteoblast. **(E)** Long-term anchoring of an HSPC on an osteoblast (see corresponding Video 2). Scale bars = 50 µm.

and was restricted in the magnupodium with the centrosome (Fig. 3 B). Microtubules emanated from the magnupodium and lined up along the cell membrane and all around the nucleus. In particular, microtubules accumulated in the wide cleft of the nucleus facing the protrusion, suggesting that microtubules were applying pushing forces responsible for the deformation of the nucleus and its separation from the centrosome (Figs. 3 C and S2 A). No separation between the centrosome and the nucleus were observed when HSPCs were plated on a nonadherent surface (i.e., in a microwell coated with PAA; see Fig. S2, C and D).

HSPC polarization was further characterized using other classic markers of polarized compartments in lymphocytes, such as uropod or immune synapse (Sánchez-Madrid and Serrador, 2009; Ritter et al., 2013). Polarized HSPCs showed accumulation of dense actin networks in the magnupodium and in a tail-like structure at the opposite side (Figs. 3 D and S2 B). Arp2/3 appeared to be concentrated in both the magnupodium and the tail (Fig. 3 D). By contrast, the phosphorylated form of myosin II and Ezrin were concentrated in the magnupodium only (Fig. 3 D). CD133/Prominin-1, a marker of HSPC magnupodium or uropod (Giebel et al., 2004; Freund et al., 2006; Bauer et al., 2008; Fonseca et al., 2010), was also concentrated in the protrusion contacting the osteoblast, further confirming its identity as a magnupodium (Fig. 3 E).

Interestingly, CD44, a well-characterized uropod marker (Gómez-Móuton et al., 2001; Freund et al., 2006), was absent from the magnupodium but localized in the tail-like protrusion at the other side of the cell (Fig. 3 F). Considering also that in these conditions HPSCs were not actively migrating, and were sometimes orthogonal to the dorsal surface of the osteoblasts (Fig. 3 A), the magnupodium could not be confused with the uropod at the rear of a migrating lymphocyte. These markers

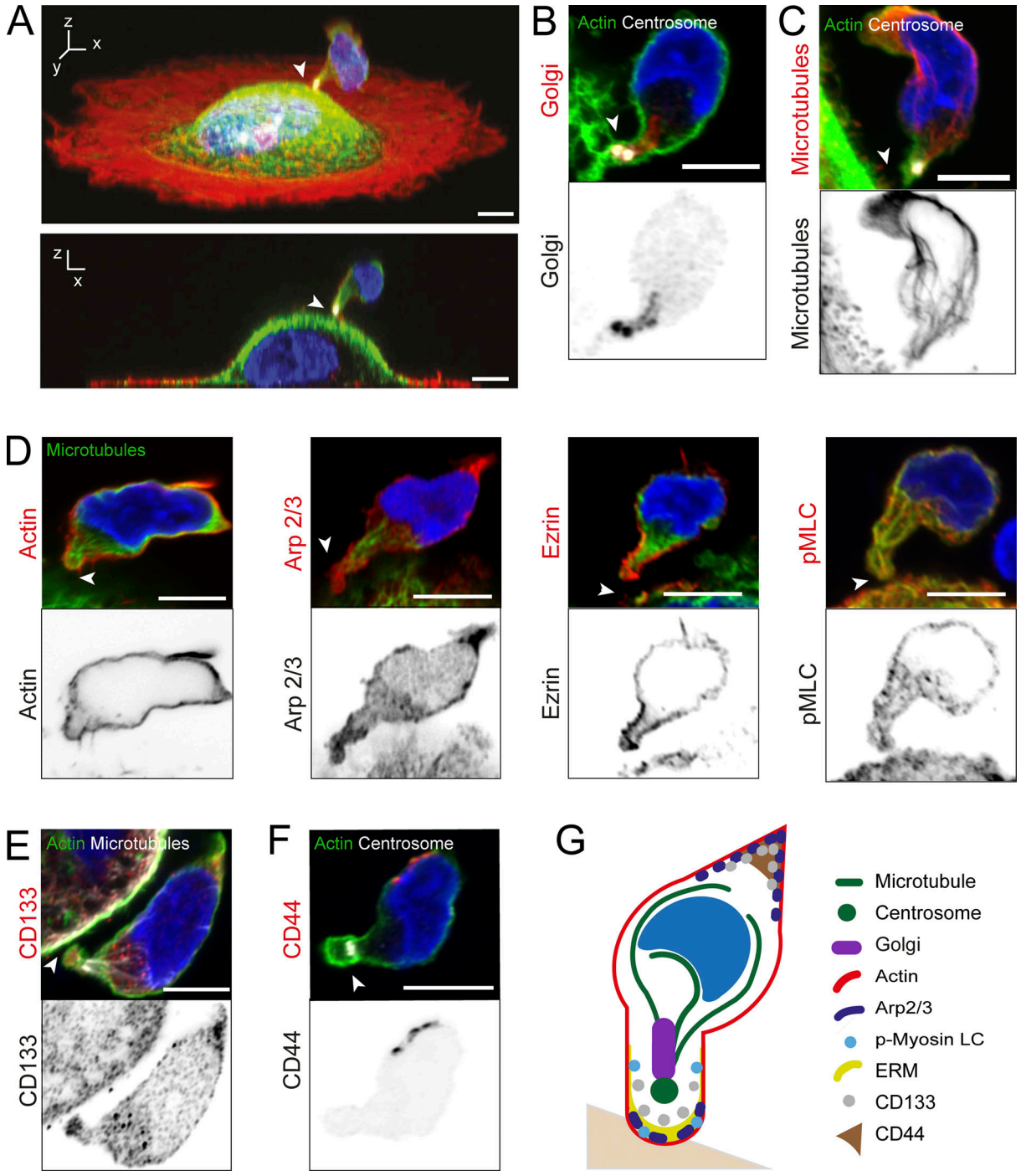

Figure 3. **HSPCs polarize upon interaction with osteoblasts. (A)** Representative confocal images of an HSPC cultured on an osteoblast in a microwell. Upper panel: Tilted 3D view. Lower panel: Lateral view. Actin appears in red, microtubules in green, DNA in blue, and centrosome in white. The HSPC is polarized, with its centrosome proximal to the point of contact with the osteoblast, highlighted with an arrow, as in all images. Scale bars = 5 µm. **(B)** Golgi organization in a polarized HSPC. Selected Z stacks of a representative cell. Upper panel: Golgi appears in red, actin in green, centrosome in white, and DNA in blue. Lower panel: Inverted image of the Golgi. Scale bar = 5 µm. **(C)** Microtubule organization in a polarized HSPC. Selected Z stacks of a representative cell. Upper panel: Microtubules appear in red, actin in green, centrosome in white, and DNA in blue. Lower panel: Inverted image of the microtubules. Scale bar = 5 µm. **(D)** Actin cytoskeleton organization in a polarized HSPC. Selected Z stacks of representative cells are presented. In all images, microtubules are in green and DNA in blue. First column: Actin appears in red in the upper panel, and the lower panel contains an inverted image of Actin. Second column: Arp2/3 appears in red in the upper panel, and the lower panel contains an inverted image of Arp2/3. Third column: Ezrin appears in red in the upper panel, and the lower panel contains an inverted image of Ezrin. Fourth column: phospho-myosin light chain appears in red in the upper panel and in black in the lower panel (inverted image). Scale bars = 5 µm. **(E)** Localization of CD133 in a polarized HSPC. Selected Z stacks of a representative cell. Upper panel: CD133 appears in red, actin in green, microtubules in white, and DNA in blue. Lower panel: Inverted image of CD133. Scale bar = 5 µm. **(F)** Localization of CD44 in a polarized HSPC. Selected Z stacks of a representative cell. Upper panel: CD44 appears in red, actin in green, centrosome in white, and DNA in blue. Lower panel: Inverted image of CD44. Scale bar = 5 µm. **(G)** Graphical summary of the localization of the factors described in a polarized HSPC.

suggested that the anchorage function, the architecture, and the molecular composition of the magnupodium more resemble an immune synapse, despite some differences, such as its size and morphology. Altogether, these results showed that HSPCs developed highly polarized cytoskeleton and membrane-associated architectures in response to forming a contact with an osteoblast (Fig. 3 G).

The similarity with some key features of immune synapses raised the question of the specificity of the target cell and prompted us to test whether HSPCs could polarize in contact with any type of stromal cell, and whether this polarization was an exclusive feature of a progenitor cell. We thus compared the polarization of HSPCs ($CD34^+$) on human umbilical vein endothelial cells (HUVECs), human bone-derived osteoblasts (hFOB cells), human skin fibroblasts (BJ cells), and murine liver–derived mesenchymal stromal cells (Fig. 4 A). As previously described, adherent cells were plated first, and HSPCs were added after. 15 h later, cells were fixed and stained to assess cell shape and centrosome positioning. To quantify HSPC polarization toward the contact site, we measured the cell polarity index, defined as the ratio between the centrosome distance to the contact site with respect to cell length (Fig. 4 B). A value close to 0 attested to a cell with the centrosome close to the contact site, whereas a value close to 1 attested to a cell with the centrosome on the other side, opposite the contact site (Fig. 4 B). Interestingly, polarization was observed when an HSPC formed a contact with a HUVEC or osteoblast, but not when in contact with a skin fibroblast (Fig. 4 C).

To assess whether polarization was related to a functional role that stromal cells have on HSPC regeneration potential, we compared the polarization of HSPCs with two murine fetal-derived stromal cell lines: AFT024, which is known to support HSPC regeneration capacities ex vivo, and BFC012, which does not (Moore et al., 1997; Charbord et al., 2014). In support of this notion, HSPCs polarized only when in contact with AFT024 cells (Fig. 4 D). We further assessed the selectivity of the polarizing interaction, in terms of the differentiation status of the hematopoietic cell, by comparing human HSCs ($CD34^+/CD38^{low}$), common myeloid progenitors (CMP; $CD34^+/CD38^+/CD33^+$; Fig. S3), activated and nonactivated primary T lymphocytes ($CD3^+$), primary monocytes ($CD14^+$), and a line of immortalized T lymphocytes (Jurkat cells) in contact with osteoblasts. We found that for both types of progenitor cells (HSCs and CMPs), when in contact with osteoblasts, marked polarization was observed (Fig. 4 E). By contrast, for primary lymphocytes, monocytes, and immortalized T cells, no polarization was observed (Fig. 4, E and F), even though primary and immortalized T cells display clear centrosome polarization when in contact with antigen-presenting cells (Yi et al., 2013; Ueda et al., 2011). Altogether, these results showed that hematopoietic polarization is not a generic outcome but is specific to defined interactions between hematopoietic progenitors and stromal cells. The results also suggested that when in contact with a stromal cell, a stem cell is more likely to polarize than a differentiated cell, and that the capacity to induce polarization of an HSPC is greater for a stromal cell from the bone marrow niche than other stromal cells. Hence, the polarization of an HSPC by a stromal cell may be induced by defined combination of surface ligands and receptors.

Several pathways are involved in the physical interaction and biochemical crosstalk between hematopoietic progenitors and niche cells (Wilson and Trumpp, 2006; Ceafalan et al., 2018). To identify those that were involved in the polarization of HSPCs, we immunolabeled receptors known to play key roles in cell adhesion, the regulation of hematopoietic differentiation (Ceafalan et al., 2018), and polarization of natural killer cells (Gross et al., 2010), including the receptor pairings: vascular cell adhesion molecule (VCAM) with VLA4, ICAM-1 with LFA-1, and SDF1 with CXCR4. All receptors appeared to be polarized and localized in the magnupodium of an HSPC with the osteoblast (Fig. 5 A). To further investigate the independent impact of a specific pathway, HSPCs were seeded into microwells, the bottoms of which were coated only with ligands of a particular receptor (Fig. 5 B and Fig. S1, B and C). HSPCs attached to the bottom of the microwell adopted the same type of elongated shapes that were observed for the contacts with osteoblasts (Fig. 5 C). This was observed with the ligands SDF1, ICAM-1, and VCAM-1, but not with the negative controls of nonadherent PAA (Fig. 5 D). Strikingly, the centrosome and microtubules were polarized only in the HSPCs in contact with SDF1, and not with ICAM-1, VCAM-1, or PAA or no coating (Fig. 5 E). These results show that although all receptors appeared to be engaged in the anchoring process (by localization), only SDF1 appeared sufficient to autonomously induce the morphologic and internal polarization of the HSPCs.

We blocked the interaction between SDF1 and CXCR4 by treating HSPCs plated on SDF1-coated surfaces with 100 µM of AMD3100, an antagonist of CXCR4 (Schols et al., 1997). This completely abolished the polarization of HSPCs (Fig. 5, F and G). We further investigated the contribution of SDF1 by comparing its expression in stromal cells capable or not of inducing the polarization of HSPCs. Immunofluorescence stainings revealed clear localization of SDF1 at the surface of osteoblasts, but lower concentrations on the surface of endothelial cells and skin fibroblasts (Fig. 5 H). This was further confirmed by measuring the quantity of proteins in Western blots (Fig. 5 I). The treatment of HSPCs in contact with osteoblasts with CXCR4 inhibitor significantly reduced their polarization (Fig. 5 J) but did not fully randomize it as it did in HSPCs plated on SDF1-coated surfaces. This showed that although SDF1 was the only ligand we tested that was capable of autonomously polarizing HSPCs, other ligands are likely involved in the case of HSPC interaction with osteoblasts.

Discussion

In modeling the bone marrow niche in vitro, we have identified novel cytoskeletal architectures and molecular signatures characterizing the interaction and polarization of the HSPC when it forms a contact with an osteoblast or endothelial cell. The shape of the pseudopod and its anchoring role are reminiscent of the previously described magnupodium (Francis et al., 1998; Freund et al., 2006). However, our results differ from the morphologic polarization of an HSPC undergoing

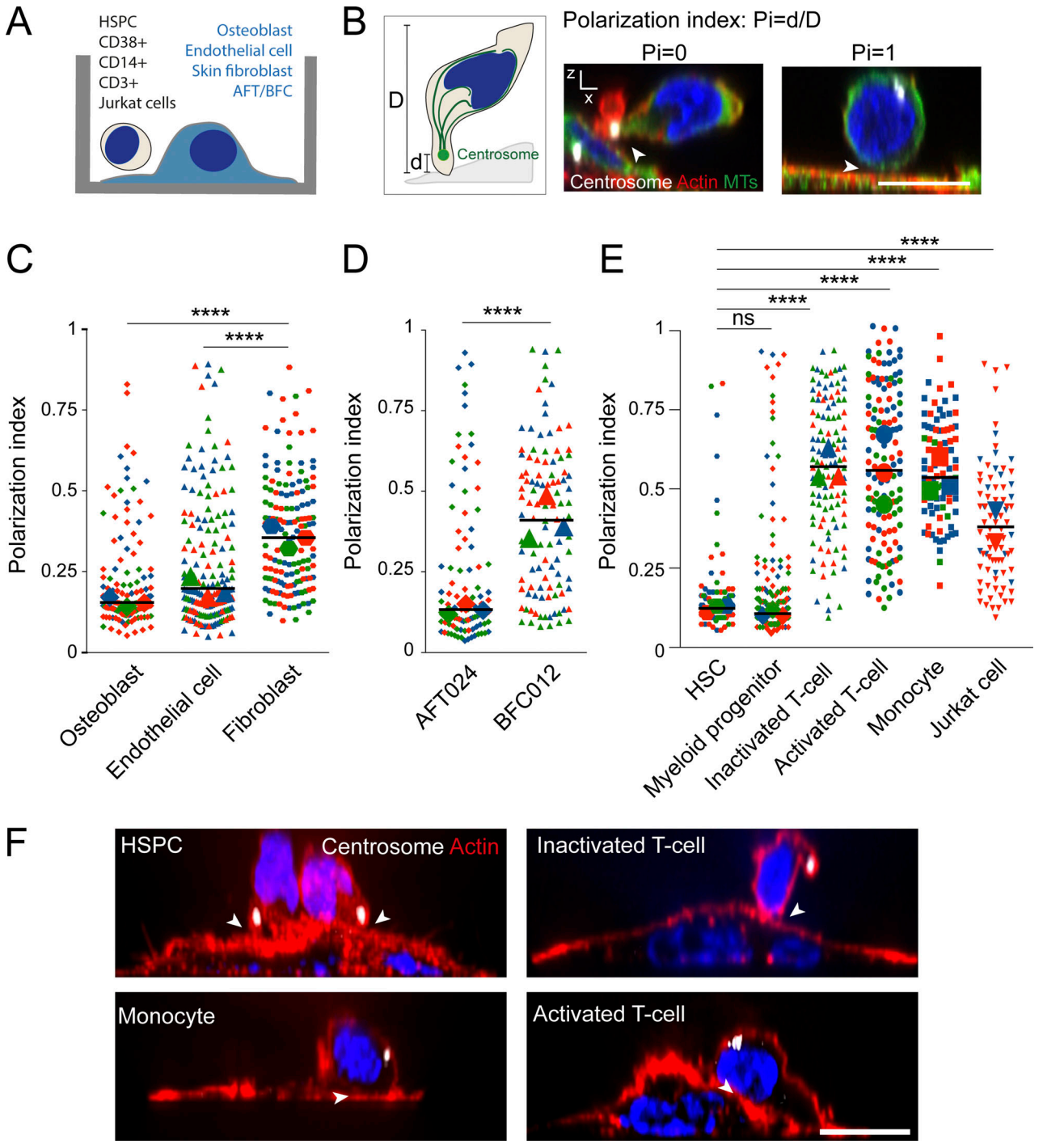

Figure 4. **HSPCs polarize upon specific heterotypic interactions. (A)** Schematic description of the experimental system to evaluate interactions between different stromal or nonstromal cell types of interest (listed in blue) and different hematopoietic cell types isolated at different stages of differentiation (listed in black). **(B)** As schematized, the HSPC polarization index (Pi) was defined as the ratio between the distance from the point of contact to the centrosome (*d*) and the HSPC length (*D*). Representative images of HSPCs with a Pi close to 0 (left) and or close to 1 (right). Actin filaments appear in red, microtubules in green, the centrosome in white, and DNA in blue. Arrowheads highlight the point of contact. Scale bar = 5 µm. **(C)** SuperPlot of the polarization index of HSPCs in contact with osteoblasts, endothelial cells, and skin fibroblasts. Each color represents a biological replicate (three replicates; osteoblasts hFOB n_{total} = 135, endothelial cells HUVEC, n_{total} = 178, and skin fibroblasts BJ, n_{total} = 149). For each replicate, the median appears as a large diamond, triangle, or hexagon with the corresponding color. The mean of the medians appears as a black bar. ****, P < 0.0001; Kruskal–Wallis ANOVA. **(D)** SuperPlot of polarization index of HSPCs in contact with mouse liver–derived stromal cell lines that either support HSPC regeneration capacities (AFT024) or not (BFC012). Each color represents a biological replicate (three replicates; AFT, n_{total} = 99; BFC, n_{total} = 106). For each replicate, the median appears as a large diamond or triangle of the corresponding color. The mean of the medians appears as a black bar. ****, P < 0.0001; Kruskal–Wallis ANOVA. **(E)** SuperPlot of polarization index of HSCs ($CD38^-$, n_{total} = 97), CMPs ($CD38^+/CD33^+$, n_{total} = 140), primary human monocytes ($CD14^+$, n_{total} =85), nonactivated ($CD3^+$, n_{total} = 115) or activated ($CD3^+$, n_{total} = 138) T cells, and immortalized T lymphocytes (Jurkat cells, n_{total} = 82) in contact with osteoblasts. Each color represents a biological replicate (three

replicates). For each replicate, the median appears as a large hexagon, diamond, triangle, disk, square, or inverted triangle of the corresponding color. The mean of the medians appears as a black bar. ****, P < 0.0001; Kruskal–Wallis ANOVA. **(F)** Representative images of HSPC/CD34⁺ (upper left), monocyte (lower left), inactivated T cell (upper right,) and activated T cell (lower right) interacting with osteoblasts. Actin appears in red, centrosome in white, and DNA in blue. Arrowheads highlight the point of contact. Scale bar = 10 µm.

migration, which, at its rear edge, assembles a protrusion that shares many features with the uropod of migrating lymphocytes or neutrophils (Fonseca et al., 2010; Görgens et al., 2012). With the formation of a long-lasting contact with stromal cells (Fig. 2 E), the hyaluronic acid receptor CD44, which is a characteristic marker of the lymphocyte and HSPC uropod (Gómez-Móuton et al., 2001; Wagner et al., 2008), was not localized at the anchorage site, but in the protrusion at the other side of the cell (Fig. 3 F). The close contact of the centrosome and Golgi apparatus to the anchorage point rather resembles the internal architecture of an immune synapse, with the exception of Golgi elongated shape (Stinchcombe et al., 2006; Ritter et al., 2013). However, the absence of HSPC spreading on the contacted cell, the pointed morphology and small size of the anchoring region, and the absence of implication of antigen processing differ from an immune synapse. Nevertheless, the location of signaling receptors on both sides of the interface (Fig. 5 A) are suggestive of specific molecular exchange between the two cells (Gillette et al., 2009). Whether this magnupodium is more than an anchoring structure and acts as a "hematopoietic synapse" conveying signals between HSPCs and specific stromal cells of the bone marrow deserves further investigation.

Indeed, HSPCs polarized in contact with specific cells by engaging a restricted set of signaling molecules. Only multipotent hematopoietic cells displayed this polarity, which could not be observed in primary lymphoid or myeloid cell types (Fig. 4 E). Furthermore, the polarization could not take place in contact with fibroblast or fetal-derived stromal cell lines that were not capable of supporting HSPC regeneration capacities (Fig. 4, C and D). Although intercellular adhesion molecule ICAM, VCAM, and CXCR4 were all segregated in the magnupodium, ICAM- and VCAM-mediated adhesions appeared to have the capacity only to induce a morphological polarization of HSPCs, whereas CXCR4 engagement with its ligand SDF1 appeared also to have the capacity to induce the recruitment of the centrosome at the contact site. However, considering that CXCR4, ICAM, VCAM, and other adhesion receptors mutually activate each other (Peled et al., 2000; Glodek et al., 2007; Petty et al., 2009; Chang et al., 2016), it is likely that the complete molecular mechanism inducing and establishing the entire internal polarization of HSPCs involves the synergy of several signaling pathways associated with the adhesion of HSPCs to bone marrow niche cells. Interestingly, SDF1, the ligand that binds to CXCR4, is a major regulator of several key features of HSPC function, including chemotactic mobilization toward the vascular niche and maintenance of the pool of HSPCs (Lévesque et al., 2003; Crane et al., 2017; Greenbaum et al., 2013). It is interesting to consider that the polarization and anchoring we identified here could be involved in the homing and tethering of HSPCs to a particular aspect of the bone marrow niche, where cells could engage specific and short-range crosstalk.

The strong polarization we observed in HSPCs is similar to several other types of stem cells in their niches (Ceafalan et al., 2018). Centrosome localization at the point of contact with anchoring cells could participate in the regulation of subsequent stem cell divisions (Yamashita et al., 2003). Thus, it is tempting to consider that the structural reorganization of intracellular and surface components of HSPCs in response to their interaction with specific niche cells regulates the quiescence and/or the asymmetry of subsequent HSPC divisions (Ho and Wagner, 2007) and thus impacts the composition and diversity of the blood lineages they generate.

Materials and methods

Cells and culture

Human umbilical cord blood samples were obtained from the Cord Blood Bank of the Saint-Louis Hospital in accordance with French national law (Bioethics Law 2011-814) and under declaration to the French Ministry of Research and Higher Studies. Using lymphocyte separation medium (Eurobio), mononuclear cells were collected using Ficoll separation medium (Eurobio). CD34⁺ HSPCs were separated from other cells by magnetic sorting, using CD34 antibodies coupled with magnetic beads (Miltenyi Biotec). Cells were used directly after isolation or frozen at −80°C in IMDM (Gibco) supplemented with 10% FBS and 10% DMSO (WAK Chemie Medical).

CD14⁺ monocytes and CD3⁺ T cells were obtained from peripheral blood samples of healthy donors from Etablissement Français du Sang (Paris, France). Monocytes were isolated by FACS after incubation of peripheral blood mononuclear cells (PBMCs) in PBS containing 10% human AB serum for 15 min. Human T cells were isolated from PBMCs through density gradient, magnetically sorted from PBMCs by negative selection with the Pan T Cell Isolation Kit (30-096-535; Miltenyi Biotec), and suspended in supplemented RPMI 1640. To activate T cells, purified T cells were kept at 37°C and 5% CO_2 for 48 h with or without 5 ng/ml IL-2 (11132D; BioLegend) and CD3/CD28 beads (4×10^4 beads per 10^6 cells; Thermo Fisher Scientific). After 48 h of incubation, beads were magnetically removed, and cells were washed and resuspended in supplemented RPMI 1640 at 10^6 cells/ml.

The cell lines used were hFOB (CRL-11372; ATCC) cultured in DMEM-F12 (Gibco); BJ (CRL-2522; ATCC) cultured in αMEM (Gibco); and the normal human lung fibroblast line, NHLF (CC-2512; Lonza) cultured in FGM-2 (Lonza). AFT024 and BFC024 immortalized mesenchymal stromal cell lines were obtained from Lemishka's group (Moore et al., 1997) and were cultured on gelatin-coated culture plates in DMEM (Gibco) with 50 µM β-mercaptoethanol. HUVECs (191027; Lonza) were cultured on gelatin-coated culture plates in EGM-2 (Lonza). Jurkat acute T cell leukemia cells (TIB-152; ATCC) were cultured in RPMI

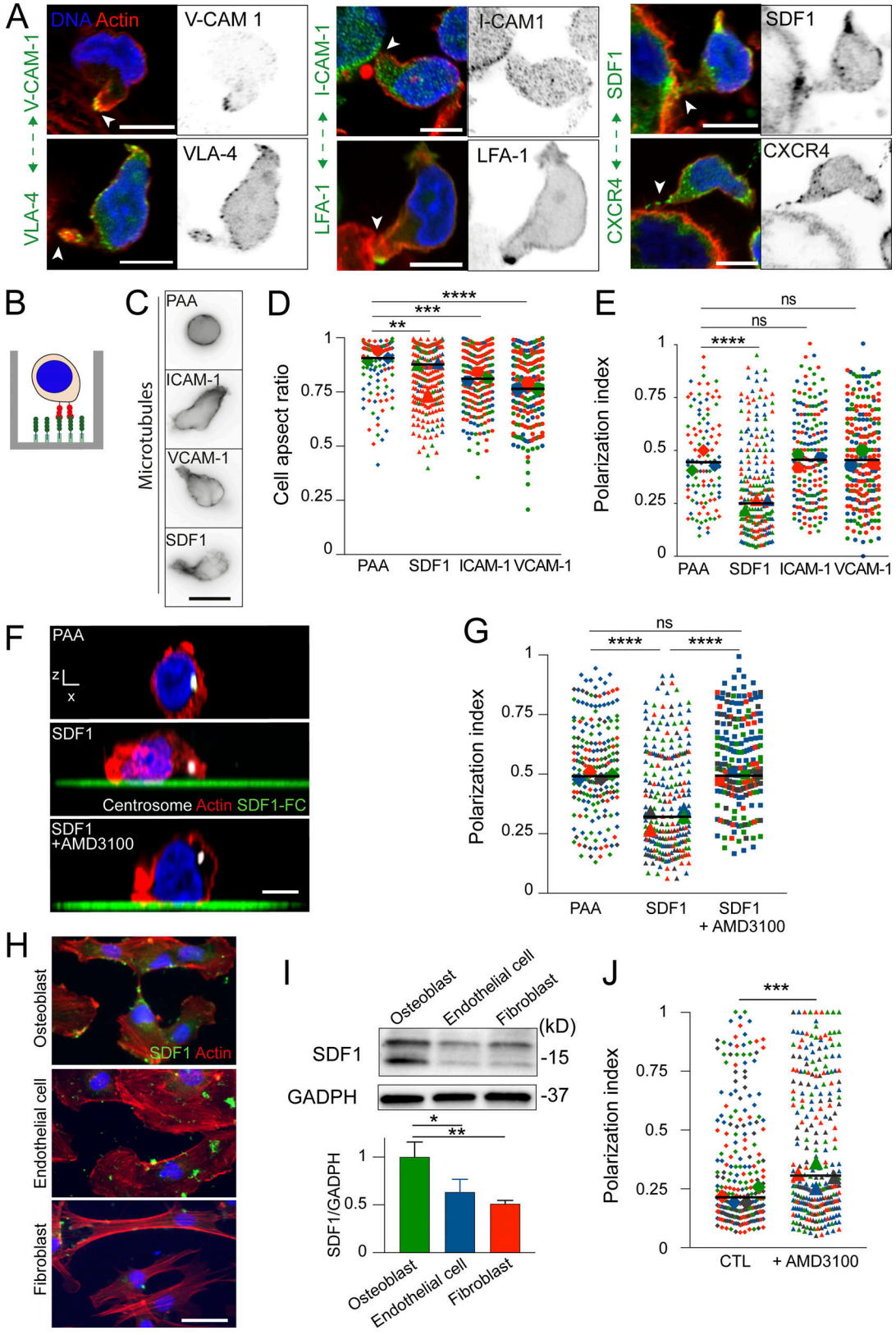

Figure 5. **Engagement of SDF1/CXCR4 is sufficient to induce HSPC polarization. (A)** Localization of ligand-receptor pairs in polarized HSPCs. Selected Z stacks of confocal images of representative cells. White arrows highlight the point of contact with the stromal cell. Actin appears in red and DNA in blue. Left: VCAM-1 and VLA-4 appear in green. Inverted images of VCAM-1 and VLA-4 are presented. Middle: ICAM-1 and LFA-1 appear in green. Inverted images of ICAM-1 and LFA-1 are presented. Right: CXCR4 and SDF1 appear in green. Inverted images of CXCR4 and SDF1 are presented. Scale bars = 5 µm. **(B)** Schematic illustration of an HSPC in a microwell coated with protein A (light green) and ligand of interest (dark green). Potentially engaged receptor is depicted in red.

(C) Representative inverted images of microtubules highlighting the shape of HSPCs cultured in uncoated (PAA), SDF1-, ICAM-1–, or VCAM-1–coated microwells. Scale bar = 5 µm. **(D)** SuperPlot of the aspect ratios of the HSPCs cultured in microwells coated with the molecules of interest. The cell aspect ratio was calculated as the ratio of the lengths of the short and long axes of the cell. Each color represents a biological replicate (three replicates: PAA n_{total} = 107, SDF1 n_{total} = 228, ICAM-1 n_{total} = 182, and VCAM-1 n_{total} = 221). For each replicate, the median appears as a large diamond, triangle, hexagon, or disk with the corresponding color. The mean of the medians appears as a black bar. ***, P = 0.0006; Kruskal–Wallis ANOVA. **(E)** SuperPlot of the polarization index of HSPCs cultured in microwells coated with the molecules of interest. Each color represents a biological replicate (three replicates: PAA n_{total} = 107; SDF1 n_{total} = 228; ICAM-1 n_{total} = 182, and VCAM-1 n_{total} = 221). For each replicate, the median appears as a large diamond, triangle, hexagon, or disk with the corresponding color. The mean of the medians appears as a black bar. ****, P < 0.0001; Kruskal–Wallis ANOVA. **(F)** Orthogonal view of representative images of an HSPC cultured in microwells coated with PAA, SDF1-FC alone, and SDF1-FC in the presence of AMD3100 (100 µM). Actin appears in red, the centrosome in white, DNA in blue, and SDF1-FC in green. Scale bar = 5 µm. **(G)** SuperPlot of the polarization index of HSPCs cultured in microwells coated with PAA, SDF1-FC alone, and SDF1-FC in the presence of AMD3100 (100 µM). Each color represents a biological replicate (four replicates: PAA n_{total} = 203; SDF1 n_{total} = 231; and SDF1-FC + AMD3100 (100 µM) n_{total} = 219). For each replicate, the median appears as a large diamond, triangle, or square with the corresponding color. The mean of the medians appears as a black bar. ****, P < 0.0001; Kruskal–Wallis ANOVA. **(H)** Representative images of osteoblasts (hFOB), endothelial cells (HUVEC), and fibroblasts (BJ) immunostained for SDF1 (in green). Actin appears in red and DNA in blue. Scale bar = 20 µm. **(I)** Upper panel: Representative immune blot performed on osteoblasts, endothelial cells, and fibroblast lysates, using anti-SDF1 and anti-GADPH antibodies. Lower panel: Quantification of the immunoblots from three independent experiments. The ratio of signal intensities of SDF1 on GADPH are normalized to the value obtained in osteoblasts. Mean values are presented. Errors bars are SD. *, P = 0.036; **, P = 0.006; unpaired *t* test. **(J)** SuperPlot of the polarization index of HSPCs cultured on osteoblasts in the absence (CTL) or presence of AMD3100 (100 µM). Each color represents a biological replicate (four replicates: CTL n_{total} = 249 and AMD3100 n_{total} = 266). For each replicate, the median appears as a large diamond, or triangle with the corresponding color. The mean of the medians appears as a black bar. ***, P = 0.0003; Mann–Whitney *U* test.

1640 (Gibco). All media were supplemented with 10% FBS and antibiotics/antimycotic (Sigma-Aldrich), except EGM2, which was supplemented with the EGM2 BulletKit (Lonza).

Flow cytometry

HSPCs were stained for 30 min at 4°C in 500 µl of PBS with 2 mM EDTA. Mouse anti-CD45-AF700 (304024; BioLegend), mouse anti-CD38-PerCp5.5 (303522; BioLegend), mouse anti-CD34-APC (555824; BD Bioscience), mouse anti-CD33-PE (555450; BD Bioscience), and mouse anti-CD19-FITC (555412; BD Bioscience) were used at 5 µl/10^6 cells. The sorting procedure was performed on a FACS Aria II with DIVA software (BD Bioscience). For monocytes, PMBCs were labeled with mouse anti-CD3-PE (clone UCTH1; 300456; BioLegend), mouse anti-CD19-PE (clone HIB19; 982402; BioLegend), mouse anti-NKp46-FITC (clone 9E2; 331921; BioLegend), mouse anti-CD16-PerCP (clone 3G8; 302029; BioLegend), or mouse anti-CD14-APC (clone M5E2; 982508; BioLegend) for 30 min on ice. The cell sorting was performed by negative selection on the BD FACS Aria III with DIVA software (BD Bioscience; see also Merah-Mourah et al. [2020]). After cell sorting, cells were centrifuged and resuspended in the desired volume of IMDM for HSPCs and RPMI 1640 for monocytes to achieve the appropriate cell culture density.

Mold fabrication for bone-marrow-on-a-chip and microwells

Maskless lithography for the manufacturing of bone-marrow-on-a-chip has been described in detail (Souquet et al., 2021): microwell shape, size, and arrangement were drawn using the software CleWin and etched in the chrome layer onto a quartz photomask (Toppan Photomask). A wafer with microstructures was made on silicon. Wafers were coated with a 5-µm layer of resin (SU8-3005; MicroChem; CTS). This layer was then fully exposed with UV light at 23 mJ/cm^2 (UV KUB2; Kloé) for 5 s for full polymerization. Another layer of resin of 50 µm (SU8-3050; MicroChem; CTS) was spincoated on top of the first layer. This layer was exposed through the quartz mask with 23 mJ/cm^2 UV light for 8 s for microwells or with the PRIMO (Alveole) 32 mJ/cm^2 for microfluidic chips. After development (Developer SU8; MicroChem; CTS), only the exposed structures remained. They were then hard baked for 2 h at 150°C and coated with gas-phase trichloro(perfluorooctyl)silane (Sigma-Aldrich).

For bone-marrow-on-a-chip devices, the glass wafer was countermolded with a silicone elastomer, base 9:1 cross-linker (Sylgard 184 kit, polydimethylsiloxane [PDMS]; Dow Corning), hereafter referred to as PDMS chip.

For microwells, a negative mold of the silicon wafer was made with PDMS and silanized in the same manner as the wafer. A second, positive mold of PDMS was made of the first mold, hereafter referred to as PDMS stamp. Thoroughly washed glass coverslips were plasmatized for 3 min, coated with gas-phase 3-(trimethoxysilyl)propyl methacrylate (Sigma-Aldrich), and baked at 120°C for 1 h. Coverslips were washed with ethanol before use. The PDMS stamp was plasmatized for 30 s and immediately placed on a silanized coverslip. Freshly made solution of 20% acrylamide 37.5/1 bisacrylamide (Euromedex) in MilliQ water, with 1% ammonium persulfate and tetramethylethylenediamine (Sigma-Aldrich) and 1% of photoinitiator (2-hydroxy-2-methylpropiophenone; Sigma-Aldrich) was immediately introduced by capillary action between the PDMS stamp and the glass coverslip. The sample was exposed to 23 mJ/cm^2 UV light for 5 min. After exposure, the PDMS stamp was removed in MilliQ water.

Cell culture in the bone-marrow-on-a-chip

PDMS chips were punched in the circular openings, and plasma was bound to glass coverslips. A CollFib hydrogel was made of thrombin (T6884; Sigma-Aldrich), 2 mg/ml fibrinogen (F3879; Sigma-Aldrich), and 1.6 mg/ml rat tail collagen I (1 U/ml; 502; Ibidi). 2 × 10^5 HUVECs and 1.5 × 10^5 hFOB cells were separately suspended in 20 µl of CollFib hydrogel and loaded in their respective channels in the chips, immediately after thrombin addition. NHLFs previously treated with mitomycin C were suspended in 20 µl of 1 U/ml thrombin and 3 mg/ml fibrinogen and injected in the chip. The chip was incubated for 30 min at 37°C. Osteoblasts and endothelial medium were loaded in the large channels adjacent to their respective cell type. After 72 h of

culture, CD34$^+$ HSPCs in CollFib hydrogel were loaded in the central channel. The system was fixed after 4 d of coculture.

Cell culture and drug treatment in microwells

Before use, the bottom glasses of the microwells were coated with 40 µg/ml of protein in 0.1 M $NaHCO_3$ solution for 15 min. The microwells were immersed in fibronectin (Sigma-Aldrich) to receive feeder cells or immersed sequentially with protein A (Interchim) and tag Fc proteins, SDF1-Fc, ICAM-1-Fc, or VCAM-1-Fc (Interchim), to receive HSPCs alone. Microwells were kept overnight in PBS before use for salt-equilibrium and photoinitiator detoxification. Microwells were rinsed twice in medium immediately before use. For HSPC–protein interactions, 15,000 HSPCs were directly seeded onto the chip and centrifuged to ensure that the cells entered into the microwells. For cell--cell interactions, 15,000 feeder cells were first seeded and centrifuged onto the entire chip. 1 h later, 15,000 HSPCs were seeded and centrifuged again. In some experiments, in addition to control nontreated cells, cells were treated with AMD3100 (CXCR4 antagonist; Sigma-Aldrich). AMD3100 was resuspended in sterile dH_20 to 10 mg/ml stock concentration. To evaluate the activity of AMD3100, a Transwell migration assay was performed using 5.0 µm polycarbonate membrane (Corning; not depicted). AMD3100 was diluted in supplemented IMDM in a range of concentrations (1–100 µM); 100 µM was finally chosen. HSPCs were resuspended in the IMDM with or without AMD3100 before being seeded and cultured in the microwells. Cells were fixed after 15 h of culture in microwells.

Western blot

hFOB cells, HUVECs, and BJ cells were lysed in radioimmunoprecipitation buffer (50 mM Tris-HCl, pH 7.4, 150 mM NaCl, 5 mM EDTA, 1.0% NP-40, 10% sodium deoxycholate, and 10% SDS). Cells were homogenized on ice with a cell scraper (UGAP) and centrifuged at 12,000 *g* for 15 min. The supernatant was harvested and quantified using the BCA assay, according to the manufacturer's instructions (Pierce Chemical Co.). An equal amount of protein from each cell type (30 µg/well) was resolved in 4–15% SDS-PAGE gels (Bio-Rad) and transferred to a nitrocellulose membrane in a Bio-Rad cuvette system in 25 mM Tris, 192 mM glycine, 20% (v/v) methanol, and pH 8.4 transfer buffer. Proteins were blocked during 1 h at RT with 5% lowfat milk in TBS/0.1% Tween-20 for 1 h at RT and incubated overnight with rabbit anti-SDF1 (350-NS-050; BioTechne) and rabbit anti-GAPDH (MA-515738; Invitrogen) 1:1,000 and 1:5,000, respectively. After washes, the membrane was incubated for 1 h with an appropriate secondary antibody conjugated with HRP (1:5,000; Vector). The proteins were visualized using a chemiluminescent method (ECL Clarity kit; Bio-Rad), and the images were captured and quantified with Image Lab Software (Bio-Rad).

Immunofluorescence

Cells were fixed for 15 min, after 4 d of culture for microfluidic chips and after 15 h of culture for microwells, in cytoskeleton buffer (10 mM MES, pH 6.1, 138 mM KCl, 3 mM MgCl, 2 mM EGTA, and 10% sucrose) in 2% PFA (Sigma-Aldrich) and 0.1% glutaraldehyde (Sigma-Aldrich) for cytoskeleton staining, or in 4% PFA for other antibodies. For phosphorylated myosin light chain, cells were permeabilized for 30 s in 0.5% Triton X-100 in cytoskeleton buffer. Cells were permeabilized for 10 min in 0.1% Triton X-100, except for surface markers, where permeabilization was performed after the primary antibody. Coverslips were neutralized with a solution of $NaBH_4$ (Sigma-Aldrich) for 10 min. The following primary antibodies and dilutions were used: rat anti-YL1/2 (MAB-1864; Serotech), 1:500; rabbit anti-pericentrin (ab4448; Abcam), 1:1,000; rabbit anti-CXCR4/CD184 (551413; BD Biosciences), 1:500; mouse anti-CD18 (clone TS1/18; MA-1810; Thermo Fisher Scientific), 1:500; mouse anti-CD49d (clone 9F10; 14-0499-82; Thermo Fisher Scientific), 1:500; rabbit anti-Arp2 (ab47654; Abcam), 1:500; rabbit anti-phospho Ezrin/Radixin/Moesin (3149; Cell Signaling), 1:200; rabbit anti-phospho-myosin light chain (3671; Cell Signaling), 1:50; mouse anti-CD44 (BBA10; R&D Systems), 1:500; mouse anti-CD133 (orb99113; Biorbyt), 1:200; rabbit anti-SDF1 (350-NS-050; BioTechne), 1:200; mouse anti-ICAM-1 (60299-1-Ig; Proteintech), mouse anti-VCAM-1 (MA5-11447; Invitrogen); and human anti-Giantin (A-R-H#03 TA10 hFc; Institut Curie), 1:200. Alexa Fluor 488-, 568-, or 647-conjugated goat anti-rat, human, rabbit (Life Technologies) and donkey anti-mouse (Invitrogen) secondary antibodies were used at 1:500. Alexa Fluor 488- or 647-conjugated phalloidin (Sigma-Aldrich) was used to label F-actin. Finally, cells were incubated with DAPI (Sigma-Aldrich) for 10 min to stain the nucleus. The coverslips were mounted with Mowiol (Sigma-Aldrich). In the case of the Fc-protein coating (Fig. S1, B and C), anti-human secondary antibody, which recognizes the Fc domain of the candidate proteins, was used at 1:1,000.

Microscopy

For live-cell imaging with trans illumination light, an Olympus IX83 microscope equipped with a PECON CellVivo incubation system controlling temperature (37°C) and CO_2 concentration (5%) was used. Images were acquired with a 10× 0.30-NA air objective on an ORCA-Flash4.0 Lite (Hamamatsu) camera and using MicroManager software.

For polarization index measurements, images were taken using either an Olympus BX63 microscope with a 100× 1.4-NA oil objective on a CoolSnap HQ2 (Photometrics) camera or a Nikon Ti-eclipse microscope equipped with a spinning disk (Yokogawa-CSU-X1) with a 60×, 1.5× 1.4-NA oil objective on an electron-multiplying charge-coupled device camera (Photometrics-Evolve512). MethaMorph was used as acquisition software.

For protein-coating analysis, a Nikon Ti-eclipse microscope equipped with an azimuthal total internal reflection fluorescence illumination iLas3 (Gataca) was used with a 100× 1.49-NA UApoTIRF objective on a CCD (Retiga R3) camera with MetaMorph software. MethaMorph was used as acquisition software.

Immunofluorescence images of cell architecture were acquired by laser scanning microscopy on an LSM 800 system mounted on an Axio Observer stand (Zeiss) and with a Plan Apochromat 63× 1.4-NA oil-immersion objective. An ∼8-Å digital zoom was added. Each wavelength was acquired separately with a 350-nm z-step width. Zen Blue edition software (Zeiss, v2.3) was used for acquisition.

Quantification

In the 3D images of the HSPCs, the positions of the centrosome (a), the point of contact (b), and the more distal point on the HSPC membrane from the point of contact, excluding thin membrane protrusions (c), were determined. Distance *d* was defined as the length between points a and b, and distance *D* the length between points b and c. The polarization index was calculated as *d*/*D* using ImageJ software.

All data are presented as SuperPlots (Lord et al., 2020). Each color represents a biological replicate, and the medians for each replicate and the mean of the medians are presented. The normality of data distribution was tested by Shapiro–Wilk test for further statistical test selection. The significance of difference between populations was tested using nonparametric (Kruskal–Wallis) ANOVA, Mann–Whitney *t* test, or parametric unpaired *t* test. All statistical analyses were performed with Prism software (GraphPad).

Online supplemental material

Fig. S1 schematizes the processes of fabrication and coating of microwells used in the study. Fig. S2 documents the microtubule and actin organization in multiple representative polarized or unpolarized HSPCs interacting with stromal cells. Fig. S3 shows the FACS gating strategy used for the isolation of HSPC subpopulations of the study. Video 1 shows the migration of HSPCs in the endosteal and vascular compartments of the bone-marrow-on-a-chip. Video 2 shows HSPCs anchoring to osteoblasts in a microwell. Video 3 shows a 3D reconstruction of an HSPC interacting and polarizing upon interaction with an osteoblast in a microwell.

Acknowledgments

We thank Noo-Li Jeon and Dorian Obino for providing chips and tips for the vasculogenesis on chip model; Sandrine Moutel and the platform TabIP for sharing the human anti-Giantin antibody; and David Romeo-Guitart for some Western Blot reagents and advice. We thank the Technological Core Facility (Plateforme Technologique de l'Institut de Recherche Saint Louis), Université de Paris, for technical support.

This work was funded by grants from the Agence Nationale de la Recherche (ANR-14-CE11-0012, ANR-10-IHUB-0002), the European Research Council (ERC CoG 771599), the Emergence program of the Ville de Paris, the "Coups d'Elan" prize of the Fondation Bettencourt Schueller, and the Fondation Schlumberger pour l'Education et la Recherche. T. Bessy received a PhD fellowship from the Université de Paris and the Ligue Contre le Cancer. The facility is supported by the Conseil Régional, Île-de-France, Canceropôle Ile-de-France, Université de Paris, Association Saint-Louis, Association Jean-Bernard, Fondation pour la Recherche Médicale, the French Institut National Du Cancer, and Ministère de la Recherche.

The authors declare no competing financial interests.

Author contributions: T. Bessy performed preliminary experiments and those presented in Figs. 2, 3 (A, C, D, and F), 4 (A–D and F), and 5 (A–E), with the help of L. Faivre, B. Vianay, and S. Brunet. A. Candelas performed experiments in Figs. 3 (B and E), 4 (E and F), and 5 (F–J) with the help of L. Faivre, A. Schaeffer, B. Vianay, C. Nakid-Cordero, J. Lion, and S. Brunet. B. Souquet and K. Saadallah performed experiments in Fig. 1 with the help of B. Vianay and S. Brunet. D. Cuvelier and S. Gobaa helped with the manufacturing and chemical grafting of microwells. T. Jaffredo provided fetal liver cell lines and advice on the project. M. Théry and S. Brunet conceived and directed the project. M. Théry and J. Larghero obtained funding for the project. M. Théry, S. Brunet, L. Blanchoin, and J. Larghero supervised the project. M. Théry, T. Bessy, and S. Brunet wrote the manuscript, which was further critically reviewed by all authors (C. Nakid-Cordero under the supervision of J-C. Bories and J. Lion under the supervision of N. Mooney).

Submitted: 11 May 2020
Revised: 23 July 2021
Accepted: 8 September 2021

References

Alakel, N., D. Jing, K. Muller, M. Bornhauser, G. Ehninger, and R. Ordemann. 2009. Direct contact with mesenchymal stromal cells affects migratory behavior and gene expression profile of CD133+ hematopoietic stem cells during ex vivo expansion. *Exp. Hematol.* 37:504–513. https://doi.org/10.1016/j.exphem.2008.12.005

Asada, N., Y. Kunisaki, H. Pierce, Z. Wang, N.F. Fernandez, A. Birbrair, A. Ma'ayan, and P.S. Frenette. 2017. Differential cytokine contributions of perivascular haematopoietic stem cell niches. *Nat. Cell Biol.* 19:214–223. https://doi.org/10.1038/ncb3475

Bauer, N., A.V. Fonseca, M. Florek, D. Freund, J. Jászai, M. Bornhäuser, C.A. Fargeas, and D. Corbeil. 2008. New insights into the cell biology of hematopoietic progenitors by studying prominin-1 (CD133). *Cells Tissues Organs.* 188:127–138. https://doi.org/10.1159/000112847

Bowers, M., B. Zhang, Y. Ho, P. Agarwal, C.C. Chen, and R. Bhatia. 2015. Osteoblast ablation reduces normal long-term hematopoietic stem cell self-renewal but accelerates leukemia development. *Blood.* 125:2678–2688. https://doi.org/10.1182/blood-2014-06-582924

Bruns, I., D. Lucas, S. Pinho, J. Ahmed, M.P. Lambert, Y. Kunisaki, C. Scheiermann, L. Schiff, M. Poncz, A. Bergman, and P.S. Frenette. 2014. Megakaryocytes regulate hematopoietic stem cell quiescence through CXCL4 secretion. *Nat. Med.* 20:1315–1320. https://doi.org/10.1038/nm.3707

Calvi, L.M., G.B. Adams, K.W. Weibrecht, J.M. Weber, D.P. Olson, M.C. Knight, R.P. Martin, E. Schipani, P. Divieti, F.R. Bringhurst, et al. 2003. Osteoblastic cells regulate the haematopoietic stem cell niche. *Nature.* 425:841–846. https://doi.org/10.1038/nature02040

Ceafalan, L.C., A.M. Enciu, T.E. Fertig, B.O. Popescu, M. Gherghiceanu, M.E. Hinescu, and E. Radu. 2018. Heterocellular molecular contacts in the mammalian stem cell niche. *Eur. J. Cell Biol.* 97:442–461. https://doi.org/10.1016/j.ejcb.2018.07.001

Chang, C.H., S.J. Hale, C.V. Cox, A. Blair, B. Kronsteiner, R. Grabowska, Y. Zhang, D. Cook, C.P. Khoo, J.B. Schrader, et al. 2016. Junctional Adhesion Molecule-A Is Highly Expressed on Human Hematopoietic Repopulating Cells and Associates with the Key Hematopoietic Chemokine Receptor CXCR4. *Stem Cells.* 34:1664–1678. https://doi.org/10.1002/stem.2340

Charbord, P., C. Pouget, H. Binder, F. Dumont, G. Stik, P. Levy, F. Allain, C. Marchal, J. Richter, B. Uzan, et al. 2014. A systems biology approach for defining the molecular framework of the hematopoietic stem cell niche. *Cell Stem Cell.* 15:376–391. https://doi.org/10.1016/j.stem.2014.06.005

Chou, D.B., V. Frismantas, Y. Milton, R. David, P. Pop-Damkov, D. Ferguson, A. MacDonald, Ö. Vargel Bölükbaşı, C.E. Joyce, L.S. Moreira Teixeira, et al. 2020. On-chip recapitulation of clinical bone marrow toxicities and patient-specific pathophysiology. *Nat. Biomed. Eng.* 4:394–406. https://doi.org/10.1038/s41551-019-0495-z

Christodoulou, C., J.A. Spencer, S.A. Yeh, R. Turcotte, K.D. Kokkaliaris, R. Panero, A. Ramos, G. Guo, N. Seyedhassantehrani, T.V. Esipova, et al. 2020. Live-animal imaging of native haematopoietic stem and

progenitor cells. *Nature.* 578:278–283. https://doi.org/10.1038/s41586-020-1971-z

Coutu, D.L., K.D. Kokkaliaris, L. Kunz, and T. Schroeder. 2017. Three-dimensional map of nonhematopoietic bone and bone-marrow cells and molecules. *Nat. Biotechnol.* 35:1202–1210. https://doi.org/10.1038/nbt.4006

Crane, G.M., E. Jeffery, and S.J. Morrison. 2017. Adult haematopoietic stem cell niches. *Nat. Rev. Immunol.* 17:573–590. https://doi.org/10.1038/nri.2017.53

Ding, L., T.L. Saunders, G. Enikolopov, and S.J. Morrison. 2012. Endothelial and perivascular cells maintain haematopoietic stem cells. *Nature.* 481:457–462. https://doi.org/10.1038/nature10783

Dusseiller, M.R., D. Schlaepfer, M. Koch, R. Kroschewski, and M. Textor. 2005. An inverted microcontact printing method on topographically structured polystyrene chips for arrayed micro-3-D culturing of single cells. *Biomaterials.* 26:5917–5925. https://doi.org/10.1016/j.biomaterials.2005.02.032

Dustin, M.L., O. Carpen, and T.A. Springer. 1992. Regulation of locomotion and cell-cell contact area by the LFA-1 and ICAM-1 adhesion receptors. *J. Immunol.* 148:2654–2663.

Fonseca, A.-V.V., and D. Corbeil. 2011. The hematopoietic stem cell polarization and migration: A dynamic link between RhoA signaling pathway, microtubule network and ganglioside-based membrane microdomains. *Commun. Integr. Biol.* 4:201–204. https://doi.org/10.4161/cib.4.2.14419

Fonseca, A.-V.V., D. Freund, M. Bornhäuser, and D. Corbeil. 2010. Polarization and migration of hematopoietic stem and progenitor cells rely on the RhoA/ROCK I pathway and an active reorganization of the microtubule network. *J. Biol. Chem.* 285:31661–31671. https://doi.org/10.1074/jbc.M110.145037

Francis, K., R. Ramakrishna, W. Holloway, and B.O. Palsson. 1998. Two new pseudopod morphologies displayed by the human hematopoietic KG1a progenitor cell line and by primary human CD34(+) cells. *Blood.* 92:3616–3623. https://doi.org/10.1182/blood.V92.10.3616

Freund, D., N. Bauer, S. Boxberger, S. Feldmann, U.W.E. Streller, G. Ehninger, C. Werner, M. Bornhäuser, J. Oswald, and D. Corbeil. 2006. Polarization of Human Hematopoietic Progenitors During Contact with Multipotent Mesenchymal Stromal Cells: Effects on Proliferation and Clonogenicity. *Stem Cells Dev.* 15:815–829. https://doi.org/10.1089/scd.2006.15.815

Frimberger, A.E., C.I. McAuliffe, K.A. Werme, R.A. Tuft, K.E. Fogarty, B.O. Benoit, M.S. Dooner, and P.J. Quesenberry. 2001. The fleet feet of haematopoietic stem cells: rapid motility, interaction and proteopodia. *Br. J. Haematol.* 112:644–654. https://doi.org/10.1046/j.1365-2141.2001.02542.x

Giebel, B., D. Corbeil, J. Beckmann, J. Höhn, D. Freund, K. Giesen, J. Fischer, G. Kögler, and P. Wernet. 2004. Segregation of lipid raft markers including CD133 in polarized human hematopoietic stem and progenitor cells. *Blood.* 104:2332–2338. https://doi.org/10.1182/blood-2004-02-0511

Gillette, J.M., A. Larochelle, C.E. Dunbar, and J. Lippincott-Schwartz. 2009. Intercellular transfer to signalling endosomes regulates an ex vivo bone marrow niche. *Nat. Cell Biol.* 11:303–311. https://doi.org/10.1038/ncb1838

Glodek, A.M., Y. Le, D.M. Dykxhoorn, S.Y. Park, G. Mostoslavsky, R. Mulligan, J. Lieberman, H.E. Beggs, M. Honczarenko, and L.E. Silberstein. 2007. Focal adhesion kinase is required for CXCL12-induced chemotactic and pro-adhesive responses in hematopoietic precursor cells. *Leukemia.* 21:1723–1732. https://doi.org/10.1038/sj.leu.2404769

Gobaa, S., S. Hoehnel, M. Roccio, A. Negro, S. Kobel, and M.P. Lutolf. 2011. Artificial niche microarrays for probing single stem cell fate in high throughput. *Nat. Methods.* 8:949–955. https://doi.org/10.1038/nmeth.1732

Gómez-Móuton, C., J.L. Abad, E. Mira, R.A. Lacalle, E. Gallardo, S. Jiménez-Baranda, I. Illa, A. Bernad, S. Mañes, and C. Martínez-A. 2001. Segregation of leading-edge and uropod components into specific lipid rafts during T cell polarization. *Proc. Natl. Acad. Sci. USA.* 98:9642–9647. https://doi.org/10.1073/pnas.171160298

Görgens, A., J. Beckmann, A.-K. Ludwig, M. Möllmann, J. Dürig, P.A. Horn, L. Rajendran, and B. Giebel. 2012. Lipid raft redistribution and morphological cell polarization are separable processes providing a basis for hematopoietic stem and progenitor cell migration. *Int. J. Biochem. Cell Biol.* 44:1121–1132. https://doi.org/10.1016/j.biocel.2012.03.020

Greenbaum, A., Y.M.S. Hsu, R.B. Day, L.G. Schuettpelz, M.J. Christopher, J.N. Borgerding, T. Nagasawa, and D.C. Link. 2013. CXCL12 in early mesenchymal progenitors is required for haematopoietic stem-cell maintenance. *Nature.* 495:227–230. https://doi.org/10.1038/nature11926

Gross, C.C., J.A. Brzostowski, D. Liu, and E.O. Long. 2010. Tethering of intercellular adhesion molecule on target cells is required for LFA-1-dependent NK cell adhesion and granule polarization. *J. Immunol.* 185:2918–2926. https://doi.org/10.4049/jimmunol.1000761

Guezguez, B., C.J.V.V. Campbell, A.L. Boyd, F. Karanu, F.L. Casado, C. Di Cresce, T.J. Collins, Z. Shapovalova, A. Xenocostas, and M. Bhatia. 2013. Regional localization within the bone marrow influences the functional capacity of human HSCs. *Cell Stem Cell.* 13:175–189. https://doi.org/10.1016/j.stem.2013.06.015

Guldevall, K., B. Vanherberghen, T. Frisk, J. Hurtig, A.E. Christakou, O. Manneberg, S. Lindström, H. Andersson-Svahn, M. Wiklund, and B. Önfelt. 2010. Imaging immune surveillance of individual natural killer cells confined in microwell arrays. *PLoS One.* 5:e15453. https://doi.org/10.1371/journal.pone.0015453

Heasman, S.J., L.M. Carlin, S. Cox, T. Ng, and A.J. Ridley. 2010. Coordinated RhoA signaling at the leading edge and uropod is required for T cell transendothelial migration. *J. Cell Biol.* 190:553–563. https://doi.org/10.1083/jcb.201002067

Ho, A.D., and W. Wagner. 2007. The beauty of asymmetry: asymmetric divisions and self-renewal in the haematopoietic system. *Curr. Opin. Hematol.* 14:330–336. https://doi.org/10.1097/MOH.0b013e3281900f12

Holloway, W., A.R. Martinez, D.J. Oh, K. Francis, R. Ramakrishna, and B.O. Palsson. 1999. Key adhesion molecules are present on long podia extended by hematopoietic cells. *Cytometry.* 37:171–177. https://doi.org/10.1002/(SICI)1097-0320(19991101)37:3<171::AID-CYTO2>3.0.CO;2-8

Ingavle, G., A. Vaidya, and V. Kale. 2019. Constructing 3D microenvironments using engineered biomaterials for HSC expansion. *Tissue Eng. Part B Rev.* 25:312–329. https://doi.org/10.1089/ten.TEB.2018.0286

Jing, D., A.-V. Fonseca, N. Alakel, F.A. Fierro, K. Muller, M. Bornhauser, G. Ehninger, D. Corbeil, and R. Ordemann. 2010. Hematopoietic stem cells in co-culture with mesenchymal stromal cells--modeling the niche compartments in vitro. *Haematologica.* 95:542–550. https://doi.org/10.3324/haematol.2009.010736

Jung, Y., J. Wang, A. Havens, Y. Sun, J. Wang, T. Jin, and R.S. Taichman. 2005. Cell-to-cell contact is critical for the survival of hematopoietic progenitor cells on osteoblasts. *Cytokine.* 32:155–162. https://doi.org/10.1016/j.cyto.2005.09.001

Khademhosseini, A., L. Ferreira, J. Blumling III, J. Yeh, J.M. Karp, J. Fukuda, and R. Langer. 2006. Co-culture of human embryonic stem cells with murine embryonic fibroblasts on microwell-patterned substrates. *Biomaterials.* 27:5968–5977. https://doi.org/10.1016/j.biomaterials.2006.06.035

Kiel, M.J., Ö.H. Yilmaz, T. Iwashita, O.H. Yilmaz, C. Terhorst, and S.J. Morrison. 2005. SLAM family receptors distinguish hematopoietic stem and progenitor cells and reveal endothelial niches for stem cells. *Cell.* 121:1109–1121. https://doi.org/10.1016/j.cell.2005.05.026

Kim, S., H. Lee, M. Chung, and N.L. Jeon. 2013. Engineering of functional, perfusable 3D microvascular networks on a chip. *Lab Chip.* 13:1489–1500. https://doi.org/10.1039/c3lc41320a

Kopp, H.-G., S.T. Avecilla, A.T. Hooper, and S. Rafii. 2005. The bone marrow vascular niche: home of HSC differentiation and mobilization. *Physiology (Bethesda).* 20:349–356. https://doi.org/10.1152/physiol.00025.2005

Lévesque, J.-P.P., J. Hendy, Y. Takamatsu, P.J. Simmons, and L.J. Bendall. 2003. Disruption of the CXCR4/CXCL12 chemotactic interaction during hematopoietic stem cell mobilization induced by GCSF or cyclophosphamide. *J. Clin. Invest.* 111:187–196. https://doi.org/10.1172/JCI15994

Lord, S.J., K.B. Velle, R.D. Mullins, and L.K. Fritz-Laylin. 2020. SuperPlots: Communicating reproducibility and variability in cell biology. *J. Cell Biol.* 219:e202001064. https://doi.org/10.1083/jcb.202001064

Lutolf, M.P., R. Doyonnas, K. Havenstrite, K. Koleckar, and H.M. Blau. 2009. Perturbation of single hematopoietic stem cell fates in artificial niches. *Integr. Biol.* 1:59–69. https://doi.org/10.1039/B815718A

Merah-Mourah, F., S.O. Cohen, D. Charron, N. Mooney, and A. Haziot. 2020. Identification of Novel Human Monocyte Subsets and Evidence for Phenotypic Groups Defined by Interindividual Variations of Expression of Adhesion Molecules. *Sci. Rep.* 10:4397. https://doi.org/10.1038/s41598-020-61022-1

Minc, N., D. Burgess, and F. Chang. 2011. Influence of cell geometry on division-plane positioning. *Cell.* 144:414–426. https://doi.org/10.1016/j.cell.2011.01.016

Moeller, H.C., M.K. Mian, S. Shrivastava, B.G. Chung, and A. Khademhosseini. 2008. A microwell array system for stem cell culture. *Biomaterials.* 29:752–763. https://doi.org/10.1016/j.biomaterials.2007.10.030

Moore, K.A., H. Ema, and I.R. Lemischka. 1997. In vitro maintenance of highly purified, transplantable hematopoietic stem cells. *Blood.* 89:4337–4347. https://doi.org/10.1182/blood.V89.12.4337

Morrison, S.J., and D.T. Scadden. 2014. The bone marrow niche for haematopoietic stem cells. *Nature.* 505:327–334. https://doi.org/10.1038/nature12984

Müller, E., T. Grinenko, T. Pompe, C. Waskow, and C. Werner. 2015. Space constraints govern fate of hematopoietic stem and progenitor cells in vitro. *Biomaterials.* 53:709–715. https://doi.org/10.1016/j.biomaterials.2015.02.095

Nelson, M.R., D. Ghoshal, J.C Mejías, D.F. Rubio, E. Keith, and K. Roy. 2021. A multi-niche microvascularized human bone marrow (hBM) on-a-chip elucidates key roles of the endosteal niche in hBM physiology. *Biomaterials.* 270:120683. https://doi.org/10.1016/j.biomaterials.2021.120683

Ochsner, M., M.R. Dusseiller, H.M. Grandin, S. Luna-Morris, M. Textor, V. Vogel, and M.L. Smith. 2007. Micro-well arrays for 3D shape control and high resolution analysis of single cells. *Lab Chip.* 7:1074–1077. https://doi.org/10.1039/b704449f

Orkin, S.H., and L.I. Zon. 2008. Hematopoiesis: an evolving paradigm for stem cell biology. *Cell.* 132:631–644. https://doi.org/10.1016/j.cell.2008.01.025

Peled, A., O. Kollet, T. Ponomaryov, I. Petit, S. Franitza, V. Grabovsky, M.M. Slav, A. Nagler, O. Lider, R. Alon, et al. 2000. The chemokine SDF-1 activates the integrins LFA-1, VLA-4, and VLA-5 on immature human CD34(+) cells: role in transendothelial/stromal migration and engraftment of NOD/SCID mice. *Blood.* 95:3289–3296. https://doi.org/10.1182/blood.V95.11.3289

Petty, J.M., C.C. Lenox, D.J. Weiss, M.E. Poynter, and B.T. Suratt. 2009. Crosstalk between CXCR4/stromal derived factor-1 and VLA-4/VCAM-1 pathways regulates neutrophil retention in the bone marrow. *J. Immunol.* 182:604–612. https://doi.org/10.4049/jimmunol.182.1.604

Pinho, S., and P.S. Frenette. 2019. Haematopoietic stem cell activity and interactions with the niche. *Nat. Rev. Mol. Cell Biol.* 20:303–320. https://doi.org/10.1038/s41580-019-0103-9

Ritter, A.T., K.L. Angus, and G.M. Griffiths. 2013. The role of the cytoskeleton at the immunological synapse. *Immunol. Rev.* 256:107–117.

Sánchez-Madrid, F., and J.M. Serrador. 2009. Bringing up the rear: defining the roles of the uropod. *Nat. Rev. Mol. Cell Biol.* 10:353–359. https://doi.org/10.1038/nrm2680

Schols, D., S. Struyf, J. Van Damme, J.A. Esté, G. Henson, and E. De Clercq. 1997. Inhibition of T-tropic HIV strains by selective antagonization of the chemokine receptor CXCR4. *J. Exp. Med.* 186:1383–1388. https://doi.org/10.1084/jem.186.8.1383

Sieber, S., L. Wirth, N. Cavak, M. Koenigsmark, U. Marx, R. Lauster, and M. Rosowski. 2018. Bone marrow-on-a-chip: Long-term culture of human haematopoietic stem cells in a three-dimensional microfluidic environment. *J. Tissue Eng. Regen. Med.* 12:479–489. https://doi.org/10.1002/term.2507

Souquet, B., M. Opitz, B. Vianay, S. Brunet, and M. Théry. 2021. Manufacturing a Bone Marrow-On-A-Chip Using Maskless Photolithography. Methods Mol. Biol. 2308:263–278.

Stinchcombe, J.C., E. Majorovits, G. Bossi, S. Fuller, and G.M. Griffiths. 2006. Centrosome polarization delivers secretory granules to the immunological synapse. *Nature.* 443:462–465. https://doi.org/10.1038/nature05071

Ueda, H., M.K. Morphew, R.J. Mcintosh, and M.M. Davis. 2011. CD4+ T-cell synapses involve multiple distinct stages. *Proc. Natl. Acad. Sci. USA.* 108:17099–17104. https://doi.org/10.1073/pnas.1113703108

Verovskaya, E.V., P.V. Dellorusso, and E. Passegué. 2019. Losing Sense of Self and Surroundings: Hematopoietic Stem Cell Aging and Leukemic Transformation. *Trends Mol. Med.* 25:494–515. https://doi.org/10.1016/j.molmed.2019.04.006

Wagner, W., F. Wein, C. Roderburg, R. Saffrich, A. Faber, U. Krause, M. Schubert, V. Benes, V. Eckstein, H. Maul, and A.D. Ho. 2007. Adhesion of hematopoietic progenitor cells to human mesenchymal stem cells as a model for cell–cell interaction. *Exp. Hematol.* 35:314–325. https://doi.org/10.1016/j.exphem.2006.10.003

Wagner, W., F. Wein, C. Roderburg, R. Saffrich, A. Diehlmann, V. Eckstein, and A.D. Ho. 2008. Adhesion of human hematopoietic progenitor cells to mesenchymal stromal cells involves CD44. *Cells Tissues Organs.* 188:160–169. https://doi.org/10.1159/000112821

Walenda, T., S. Bork, P. Horn, F. Wein, R. Saffrich, A. Diehlmann, V. Eckstein, A.D. Ho, and W. Wagner. 2010. Co-culture with mesenchymal stromal cells increases proliferation and maintenance of haematopoietic progenitor cells. *J. Cell. Mol. Med.* 14:337–350. https://doi.org/10.1111/j.1582-4934.2009.00776.x

Wilson, A., and A. Trumpp. 2006. Bone-marrow haematopoietic-stem-cell niches. *Nat. Rev. Immunol.* 6:93–106. https://doi.org/10.1038/nri1779

Wuchter, P., R. Saffrich, S. Giselbrecht, C. Nies, H. Lorig, S. Kolb, A.D. Ho, and E. Gottwald. 2016. Microcavity arrays as an in vitro model system of the bone marrow niche for hematopoietic stem cells. *Cell Tissue Res.* 364:573–584. https://doi.org/10.1007/s00441-015-2348-8

Yamashita, Y.M., D.L. Jones, and M.T. Fuller. 2003. Orientation of Asymmetric Stem Cell Division by the APC Tumor Suppressor and Centrosome. *Science.* 301:1547–1550. https://doi.org/10.1126/science.1087795

Yi, J., X. Wu, A.H. Chung, J.K. Chen, T.M. Kapoor, and J.A. Hammer. 2013. Centrosome repositioning in T cells is biphasic and driven by microtubule end-on capture-shrinkage. *J. Cell Biol.* 202:779–792. https://doi.org/10.1083/jcb.201301004

Supplemental material

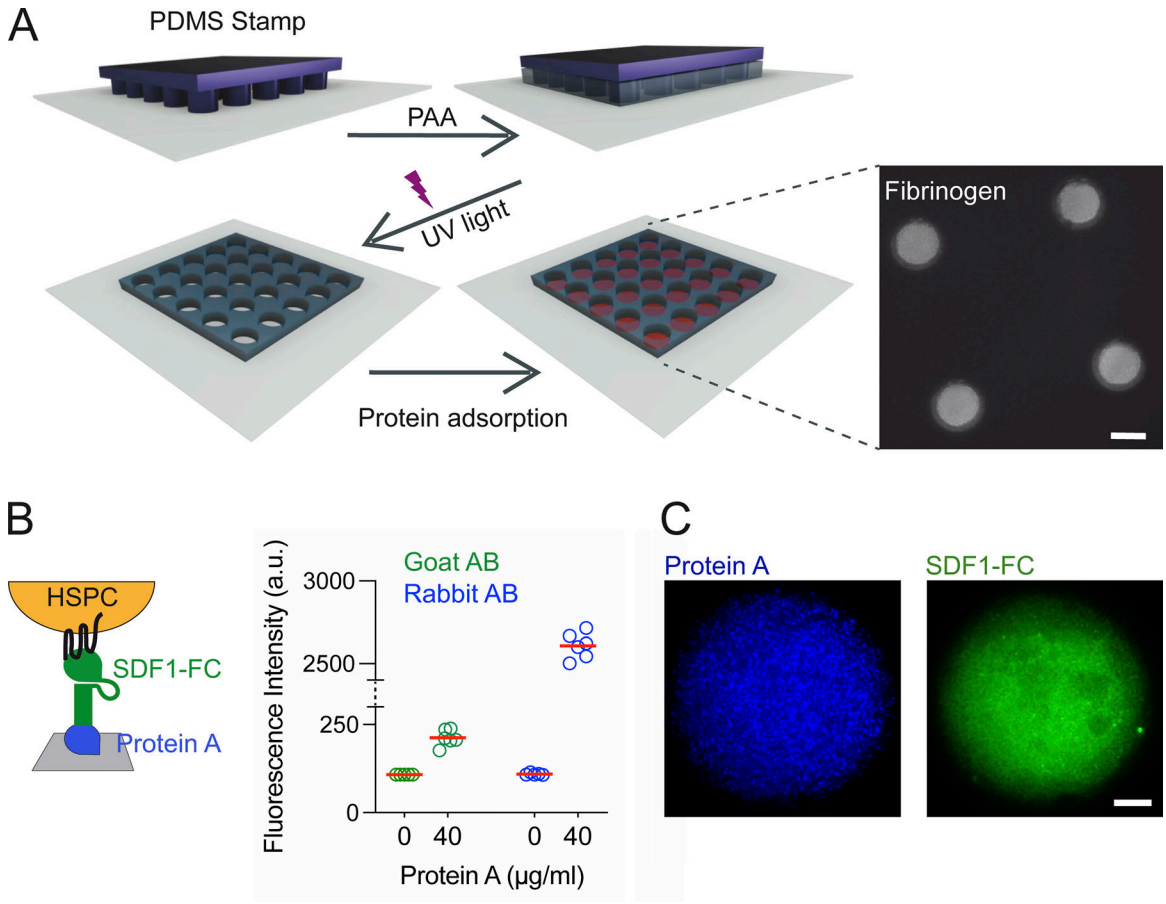

Figure S1. **Microwell manufacturing. (A)** A PDMS stamp (purple) was placed in contact with a silanized glass coverslip (gray). The acrylamide and bis-acrylamide mix (black) filled by capillarity the gap between the PDMS and the glass coverslip. The sandwich was exposed to UV for 5 min to polymerize the PAA. After removal of the PDMS mold, the glass bottom was functionalized by binding proteins to the silane (red). Left inset: Representative image of fluorescent fibrinogen in the wells. Scale bar = 50 µm. **(B)** Left: Schematic representation of the coating system in microwells. Protein A (in blue) was first coated on the coverslip (in gray). SDF1 linked to a fragment crystallizable (FC) domain, which binds to Protein A, was added on top. The ability of SDF1-FC (in green) to induce HSPC (in salmon) polarization was tested. Right: Fluorescent rabbit and goat secondary antibodies (AB) were used to validate Protein A coating in microwells. As a negative control, goat AB (in green) does not label Protein A: no fluorescence was detected in the absence or in presence of Protein A. In contrast, fluorescence was detected upon Protein A coating using rabbit AB (in blue), which does react with Protein A. This test validated Protein A coating in the microwells. **(C)** Representative image of Protein A coating (blue) detected by rabbit AB and SDF1-FC (green) attached to Protein A in a microwell. Scale bar = 10 µm.

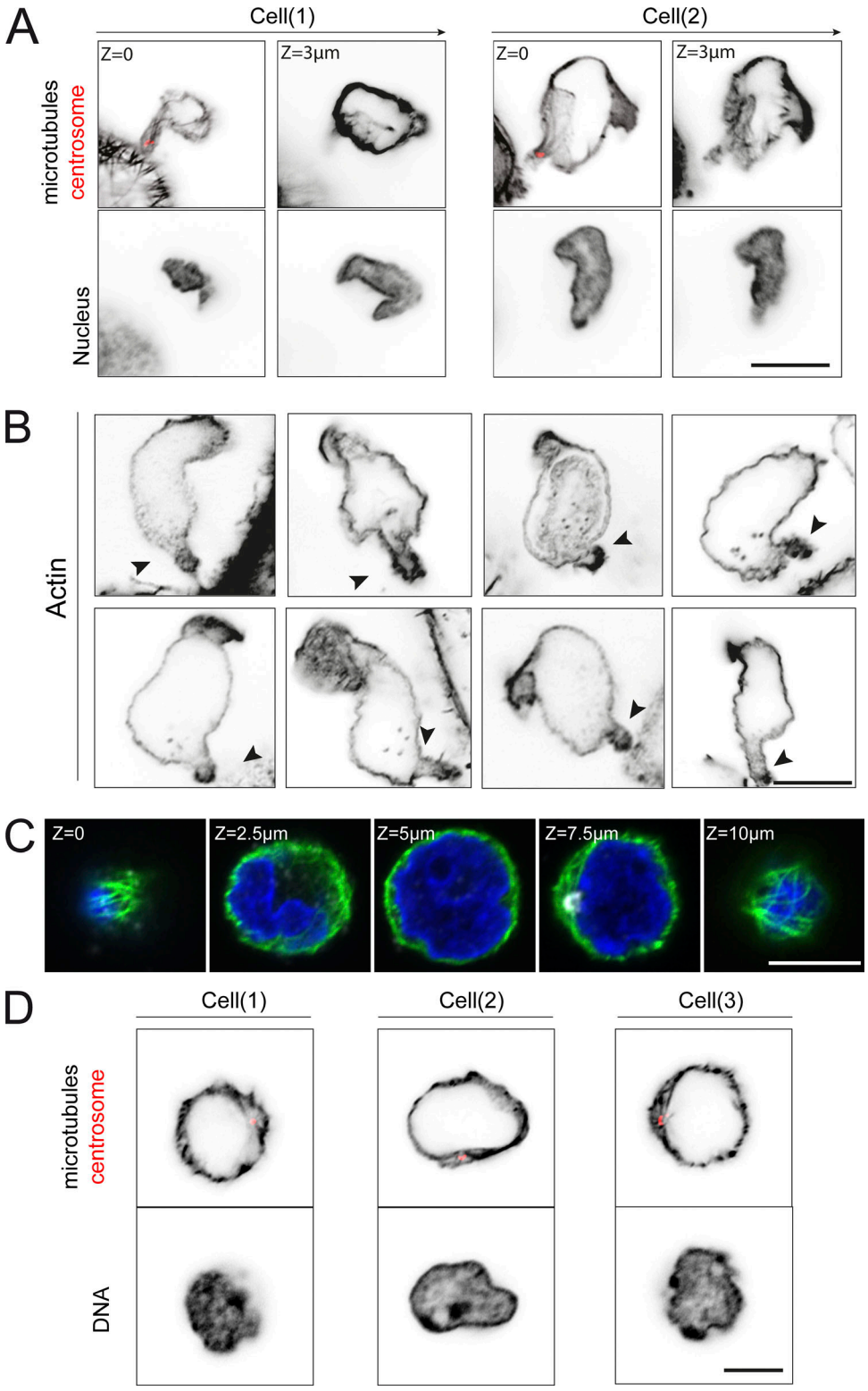

Figure S2. **Cytoskeleton architecture of HSPCs in adhesive and nonadhesive microwells. (A)** Inverted images of selected Z stacks of two representative HSPC polarized on osteoblasts. Upper panel: Microtubules appear in black and the centrosome in red. Lower panel: Nucleus (DNA staining) appears in black. **(B)** Inverted images of selected Z stacks of actin organization in representative HSPCs polarized upon contact with osteoblast. The point of contact is highlighted with a black arrow. **(C)** Cytoskeleton architecture of HSPCs in a nonadhesive microwell. Selected Z stack (z = 0–10 µm) of a representative HSPC cultured in a PAA microwell (nonadhesive). Microtubules appear in green, centrosome in white, and DNA in blue. The centrosome was tightly associated with the nucleus, and not proximal to the glass bottom. Scale bar = 5 µm. **(D)** Inverted images of representative HSPCs cultured in PAA microwells. Upper panel: Microtubules appear in black and the centrosome in red. Lower panel: Corresponding image of the nucleus. Scale bar = 5 µm.

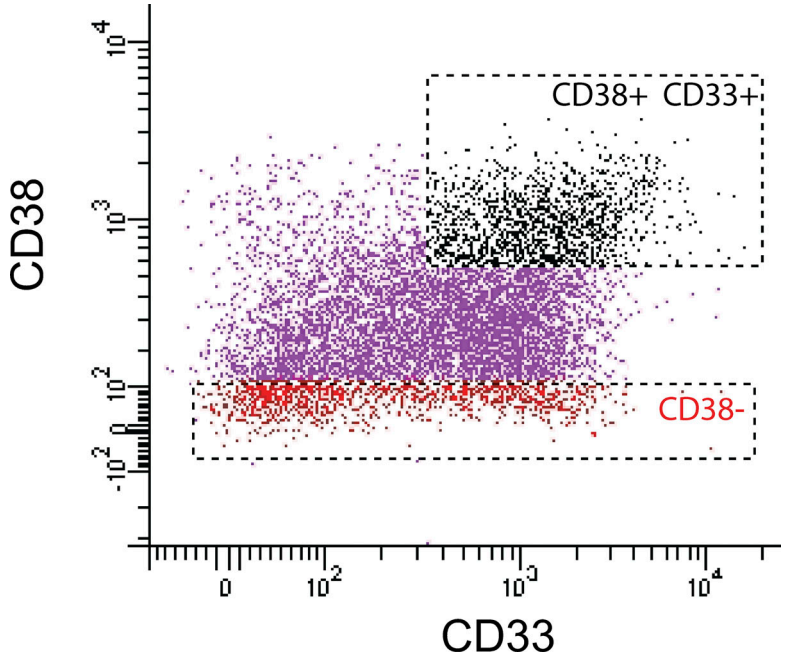

Figure S3. **FACS isolation of HSC and CMP.** FACS gating strategy to isolate, from the initial population of HSPCs ($CD34^+$ cells), $CD34^+/CD38^-$ cells (considered as more HSCs, in red), and $CD34^+/CD38^+/CD33^+$ cells (CMPs, in black).

Video 1. **HSPC migration in a bone-marrow-on-a-chip.** Video shows transmitted light (phase contrast) of an HSPC loaded in the central channel and migrating toward the pseudo-endosteal compartment (top channel), containing osteoblasts, and the pseudo-vascular compartment (bottom channel), containing endothelial cells, forming a vascular network. The pitch of central pilar spacing is 200 µm. Time is indicated in hours.

Video 2. **HSPC anchorage to osteoblasts in a microwell.** Video shows transmitted light (phase contrast) of two HSPCs on top of two osteoblasts in a microwell (50 µm wide). Note the dynamic shape changes of HSPCs but their long-lasting anchorage on the dorsal surface of osteoblasts via a thin protrusion. Scale bar represents 20 µm. Time is indicated in hours:minutes.

Video 3. **HSPC polarization in contact with an osteoblast.** Video shows the rotation of a 3D reconstruction of a Z stack. It shows a single HSPC on top of an osteoblast in a microwell. Microtubules are shown in green, actin filaments in red, and centrosomes in white. In the HSPC, note the position of the centrosome at the tip of the protrusion forming the contact with the osteoblast. The microwell diameter, and thus the width of the osteoblast, is 50 µm.